AD-A060 386 SYSTEMS RESEARCH LABS INC DAYTON OHIO RESEARCH APPLI--ETC F/G 11/2
PROPERTIES AND MICROSTRUCTURES OF HIGH-TEMPERATURE MATERIALS.(U)
AUG 78 M G MENDIRATTA, N S CHOUDHURY F33615-75-C-1005

UNCLASSIFIED SRL-3165 AFML-TR-78-112 NL

1 OF 1
AD
A060386

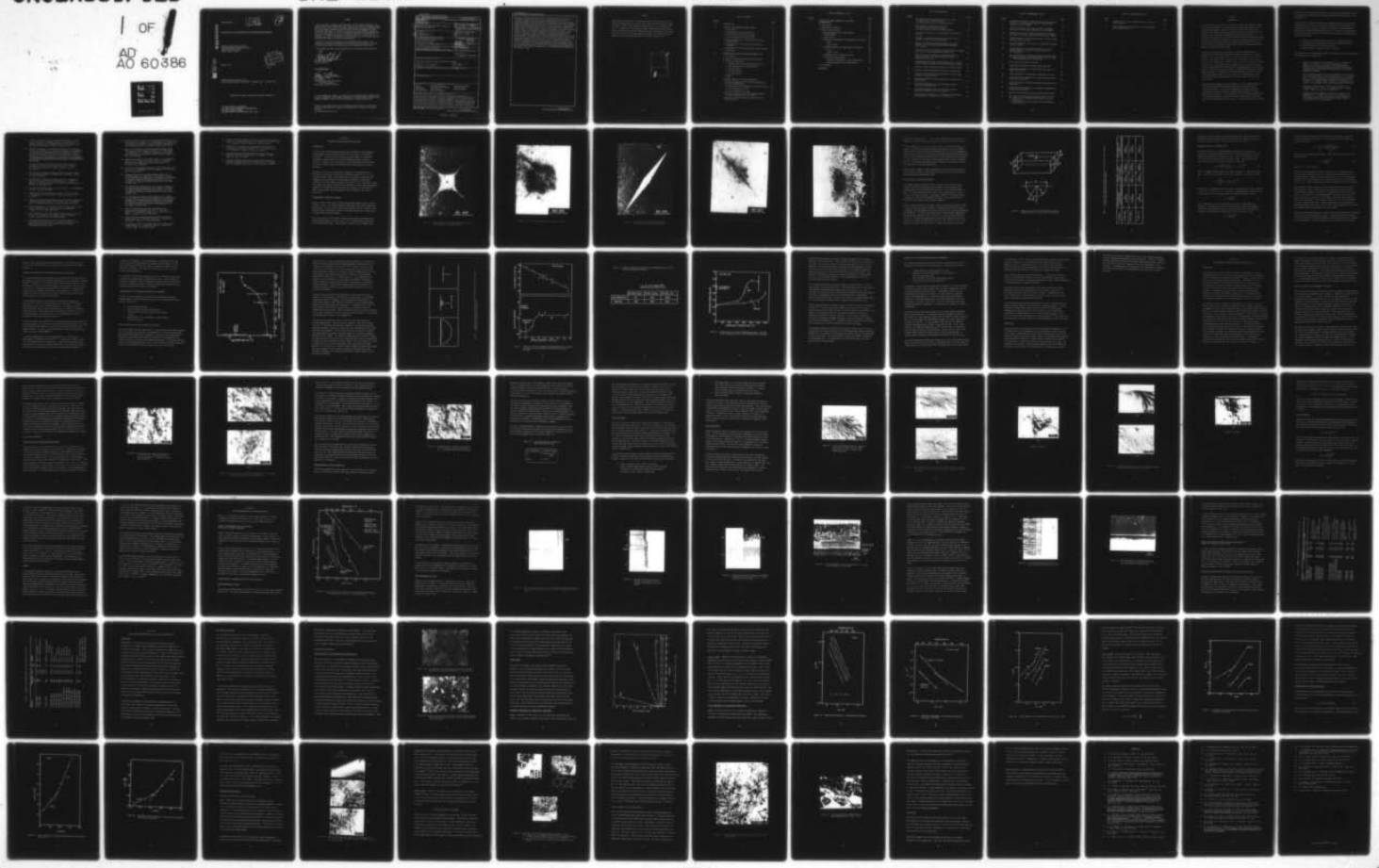

AFML-TR-78-112

LEVEL

(2)

PROPERTIES AND MICROSTRUCTURES OF HIGH-TEMPERATURE MATERIALS

Research Applications Division
Systems Research Laboratories, Inc.
2800 Indian Ripple Road
Dayton, Ohio 45440

August 1978

TECHNICAL REPORT AFML-TR-78-112
Final Technical Report for period 1 December 1974 - 31 March 1978

Approved for public release; distribution unlimited.

AIR FORCE MATERIALS LABORATORY
AIR FORCE WRIGHT AERONAUTICAL LABORATORIES
AIR FORCE SYSTEMS COMMAND
WRIGHT-PATTERSON AIR FORCE BASE, OHIO 45433

NOTICE

When Government drawings, specifications, or other data are used for any purpose other than in connection with a definitely related Government procurement operation, the United States Government thereby incurs no responsibility nor any obligation whatsoever; and the fact that the Government may have formulated, furnished, or in any way supplied the said drawings, specifications, or other data, is not to be regarded by implication or otherwise as in any manner licensing the holder or any other person or corporation, or conveying any rights or permission to manufacture, use, or sell any patented invention that may in any way be related thereto.

This report has been reviewed by the Information Office (OI) and is releasable to the National Technical Information Service (NTIS). At NTIS, it will be available to the general public, including foreign nations.

This technical report has been reviewed and is approved for publication.

DR. HARRY A. LIPSITT
Project Engineer

FOR THE COMMANDER

DR. HENRY C. GRAHAM
Acting Chief
Processing and High Temperature
Materials Branch
Metals and Ceramics Division

If your address has changed, if you wish to be removed from our mailing list, or if the addressee is no longer employed by your organization, please notify AFML/LLM, WPAFB, OH 45433 to help us maintain a current mailing list.

Copies of this report should not be returned unless return is required by security considerations, contractual obligations, or notice on a specific document.

AIR FORCE/56780/10 October 1978 — 150

UNCLASSIFIED

SECURITY CLASSIFICATION OF THIS PAGE (When Data Entered)

REPORT DOCUMENTATION PAGE

READ INSTRUCTIONS BEFORE COMPLETING FORM

1. REPORT NUMBER: AFML-TR-78-112	2. GOVT ACCESSION NO.
3. RECIPIENT'S CATALOG NUMBER	
4. TITLE (and Subtitle): PROPERTIES AND MICROSTRUCTURES OF HIGH-TEMPERATURE MATERIALS	5. TYPE OF REPORT & PERIOD COVERED: Final Technical Report, 1 Dec. 1974 - 31 March 1978
	6. PERFORMING ORG. REPORT NUMBER: 3165
7. AUTHOR(s): M. G. Mendiratta, N. S. Choudhury	8. CONTRACT OR GRANT NUMBER(s): F33615-75-C-1005
9. PERFORMING ORGANIZATION NAME AND ADDRESS: Systems Research Laboratories, Inc., 2800 Indian Ripple Road, Dayton, Ohio 45440	10. PROGRAM ELEMENT, PROJECT, TASK AREA & WORK UNIT NUMBERS: 61102F, 2306P303, P3
11. CONTROLLING OFFICE NAME AND ADDRESS: Processing and High Temperature Materials Branch, Air Force Materials Laboratory, Wright-Patterson Air Force Base, Ohio 45433	12. REPORT DATE: August 1978
	13. NUMBER OF PAGES: 86
14. MONITORING AGENCY NAME & ADDRESS (if different from Controlling Office)	15. SECURITY CLASS. (of this report): Unclassified
	15a. DECLASSIFICATION/DOWNGRADING SCHEDULE

16. DISTRIBUTION STATEMENT (of this Report)

Approved for public release; distribution unlimited.

SRL-3165 96 p.

17. DISTRIBUTION STATEMENT (of the abstract entered in Block 20, if different from Report)

18. SUPPLEMENTARY NOTES

19. KEY WORDS (Continue on reverse side if necessary and identify by block number)

Creep	Fracture Mechanics	Titanium Aluminides
Oxidation	Four-Point Bend Strength	Silicon Nitride
Fractography	Microstructure	Silicon Carbide
Controlled Flaws	Fracture Toughness	

20. ABSTRACT (Continue on reverse side if necessary and identify by block number)

This final technical report contains information on investigations whose aim was to study specific aspects of properties and microstructures of high-temperature materials. These investigations are: 1) fracture from controlled surface flaws in structural ceramics, 2) fractography of reaction-sintered silicon nitride, 3) oxidation behavior of titanium aluminides, and 4) creep behavior of Ti_3Al and Ti_3Al + 10 wt% Nb. The scientific basis and advantages and disadvantages of the microhardness indentation technique in

DD FORM 1 JAN 73 1473 EDITION OF 1 NOV 65 IS OBSOLETE

UNCLASSIFIED

SECURITY CLASSIFICATION OF THIS PAGE (When Data Entered)

titanium aluminide

409 471

78 10 20 063

producing controlled surface flaws and in studying the fracture behavior of structural ceramics are reviewed. The current applications of this technique--including fracture toughness determinations, subcritical-crack-growth measurements, and investigation of mixed-mode fracture--are discussed. An SEM fractography study has been carried out on bend bars of KBI and Norton NC-350 reaction-sintered silicon-nitride ceramics fractured at temperatures ranging from room temperature to 1500°C. The purpose of this study was to examine overall fracture features, identify and analyze the fracture-initiating critical flaws, and correlate these with four-point bend strength. The oxidation behavior of titanium aluminides is reported which includes the effect of temperature upon the oxidation of TiAl-base aluminides, the microstructural characterization of scale morphologies of both TiAl and Ti_3Al, and the results of oxidation tests on alloys of TiAl and Ti_3Al. The steady-state creep behavior of Ti_3Al and Ti_3Al + 10 wt% Nb was studied in the temperature range 550 to 825°C and in the stress range 69 to 312 MN/m^2 (10 to 45 ksi). The temperature and stress dependences of the steady-state creep rate were determined. From these dependences the creep-activation energies and stress exponents were calculated, thus establishing the phenomenology of creep behavior in Ti_3Al-base aluminides. The creep-deformation substructures were studied by TEM.

FOREWORD

This report was prepared by the Research Applications Division, Systems Research Laboratories, Inc., Dayton, Ohio, under Air Force Contract F33615-75-C-1005, Project 2306, Task P2, Work Unit 04. Dr. H. A. Lipsitt and Dr. H. C. Graham of the Processing and High Temperature Materials Branch, Air Force Materials Laboratory (AFML/LLM), Wright-Patterson Air Force Base, Ohio 45433, were the Government project monitors. The research reported herein covered the period 1 December 1974 through 31 March 1978.

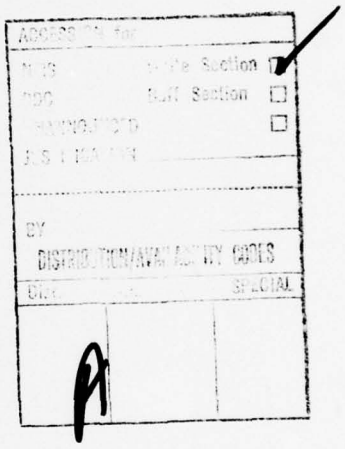

TABLE OF CONTENTS

TABLE OF CONTENTS (cont'd)

LIST OF ILLUSTRATIONS

LIST OF ILLUSTRATIONS (cont'd)

LIST OF ILLUSTRATIONS (cont'd)

Section I

INTRODUCTION

The gas-turbine engine presents to materials scientists challenging problems of materials development as a result of the stringent high-temperature and corrosive environments. Materials which can be used under these severe conditions must possess adequate mechanical properties including short- and long-term static and cyclic strength and thermal-shock resistance. In addition, these materials must exhibit adequate oxidation resistance--achieved through the formation of an adherent, continuous protective oxide scale which does not spall off during thermal cycling and can withstand hot-corrosion attacks resulting from reactions with sulfur and other contaminants ingested with inlet air and contained in fuel.

The past two decades have seen spectacular alloy-development payoffs, resulting in Ni- and Co-base superalloys capable of operation at ~ 1000°C. However, chances seem rather slim for further development of these alloys to provide a still higher temperature capability, the major reason being the rapid loss of strength above ~ 1000°C. Also, these alloys, even with coatings, may not be able to withstand the very damaging effect of oxidation and hot corrosion combined with loss of strength at high temperatures. The elements used in the Ni- and Co-base alloys are of strategic importance and are being depleted rapidly. The densities of Ni-base superalloys currently in use in gas-turbine engines range from 7.75 to 9.27 g/cc. Replacement of these alloys with lighter-weight materials will improve engine performance and fuel economy.

Significant improvements in the performance of current turbine engines can be achieved through higher operating temperatures and lower-density structural materials. It has been established that higher operating temperatures in turbine engines will significantly improve fuel economy and operating efficiency. Lower densities--or, more directly, higher ratios of strength and modulus to density--will also improve engine performance and, thus, effect significant fuel saving. This dual objective has prompted

research efforts toward the development of ceramics and intermetallics, many of which possess low densities and high strengths and inertness up to high temperatures.

At the Air Force Materials Laboratory at Wright-Patterson Air Force Base, considerable research efforts are being directed toward development of Si-bearing structural ceramics and titanium aluminides for high-temperature applications. Systems Research Laboratories, Inc. (SRL), has participated in these programs and this report includes the results of investigations in four principal areas:

1) Fracture from controlled surface flaws in structural ceramics
2) Fractography of reaction-sintered silicon nitride (RS Si_3N_4)
3) Oxidation behavior of titanium aluminides
4) Creep behavior of Ti_3Al and Ti_3Al + 10 wt% Nb

The publications and presentations which have resulted from these and related investigations are listed below.

1. "Fracture from Controlled Surface Flaws," M. G. Mendiratta (with *J. J. Petrovic*). *Accepted* for presentation and publication at the Special Session on Fracture Mechanics Tests for Brittle-Non-Metallic Materials, ASTM 11th National Symposium on Fracture Mechanics to be held 12-14 June 1978, Blacksburg, Virginia.

2. "Use of Controlled Surface Flaws in Studying Slow Crack Growth in Structural Ceramics," M. G. Mendiratta (with J. J. Petrovic and P. L. Land), presented at the 29th Pacific Coast Regional Meeting of the American Ceramic Society, San Francisco, CA, 31 October - 3 November 1976. Accepted for publication in the Journal of the American Ceramic Society, May-June 1978 issue.

3. "Compounds and Properties of the Si-Al-O-N System," N. S. Choudhury (with P. L. Land, J. M. Wimmer, and R. W. Burns), J. Amer. Ceram. Soc. 61, 56 (Jan-Feb 1978).

4. "Steady State Creep Behavior of Ti_3Al in Air and in Inert Atmosphere," M. G. Mendiratta (with S. M. L. Sastry, W. J. Yang, and H. A. Lipsitt), presented at the Annual Meeting of the Metallurgical Society of AIME, Atlanta, Georgia, 6-10 March 1977 (to be published).

5. "Effect of Temperature upon the Oxidation Behavior of Ti-36 w/o Al Alloy," N. S. Choudhury (with J. E. Henry and H. C. Graham), presented at the Annual Meeting of the Metallurgical Society of AIME, Atlanta, Georgia, 6-10 March 1977.

6. "Oxidation Behavior of Titanium Aluminides," N. S. Choudhury (with H. C. Graham and J. W. Hinze), presented at the Symposium on Properties of High-Temperature Alloys sponsored jointly by the Electrochemical Society and the Metallurgical Society of AIME held in Las Vegas, Nevada, 17-22 October 1976. Published in Proceedings of the Symposium on Properties of High Temperature Alloys (The Electrochemical Society, Princeton, NJ, March 1977), pp. 668-680.

7. "Lifetime Prediction of Brittle Materials Having Spatial Variations in Fracture Properties of K_{Ic} and v versus K_I," M. G. Mendiratta (with P. L. Land), J. Mater. Sci. 12, 1421 (1977).

8. "Dynamic K_{Ic} and Dynamic Flexural Strength in HS-130 Si_3N_4," M. G. Mendiratta (with J. M. Wimmer and I. Bransky), J. Mater. Sci. 12, 212 (1977).

9. "Fractography of Reaction-Sintered Si_3N_4," M. G. Mendiratta (with P. L. Land, R. Ruh, R. W. Rice, and D. C. Larsen), presented at the Fall Meeting of the American Ceramic Society, Hyannis, MA, September 1977.

10. "Silicon Cerium Oxynitride," R. R. Wills (with J. A. Cunningham), J. Mater. Sci. 12, 208 (1977).

11. "Fabrication of Reaction-Sintered Sialon," R. R. Wills (with J. M. Wimmer and R. W. Stewart), J. Amer. Ceram. Soc. 60, 64 (1977).

12. "Effect of Composition and X-Phase upon the Intrinsic Properties of Reaction-Sintered Sialon," R. R. Wills (with J. M. Wimmer and R. W. Stewart), Bull. Amer. Ceram. Soc. 56, 194 (1977).

13. "Phase Relationships in the System Si_3N_4-Y_2O_3-SiO_2," R. R. Wills (with S. Holmquist, J. M. Wimmer, and J. A. Cunningham), J. Mater. Sci. 11, 1305 (July 1976).

14. "The Stability of the Silicon-Yttrium Oxynitrides," R. R. Wills (with J. A. Cunningham, J. M. Wimmer, and R. W. Stewart), J. Amer. Ceram. Soc. 59, 269 (May-June 1976).

15. "Pressureless Densification in the Si-Al-O-N System," R. R. Wills (with R. W. Stewart and J. M. Wimmer), presented at the Annual Spring Meeting of the American Ceramic Society, Cincinnati, OH, 3-5 May 1976.

16. "Further Studies on the Silicon Lanthanide Oxynitrides," R. R. Wills (with R. W. Stewart, J. A. Cunningham, J. M. Wimmer, and S. Holmquist), presented at the Annual Spring Meeting of the American Ceramic Society, Cincinnati, Ohio, 3-5 May 1976.

17. "Intrinsic Properties of Reaction-Sintered Sialon and the Effect of the X and J Phase upon Them," R. R. Wills (with J. M. Wimmer and R. W. Stewart), presented at the Annual Spring Meeting of the American Ceramic Society, Cincinnati, Ohio, 3-5 May 1976.

18. "Steady State Creep of Ti_3Al-Base Alloys," M. G. Mendiratta (with S. M. L. Sastry, W. J. Yang, and H. A. Lipsitt), presented at the AIME-ASM Meeting, Niagara Falls, NY, May 1976 (to be published).

19. "The Silicon Lanthanide Oxynitrides," R. R. Wills (with R. W. Stewart, J. A. Cunningham, and J. M. Wimmer), J. Mater. Sci. 11, 749 (April 1976).

20. "Oxidation Behavior of Titanium-Aluminum Alloys," N. S. Choudhury (with J. W. Hinze and H. C. Graham), presented at the AFWAL/AIAA Mini-Symposium on New Avenues for Progress in Aerospace Research Technology and Systems, Air Force Institute of Technology, Wright-Patterson Air Force Base, 25 March 1976.

21. "The Silicon Metal Oxynitrides," R. R. Wills, presented at the AFWAL/AIAA Mini-Symposium on New Avenues for Progress in Aerospace Research Technology and Systems, Air Force Institute of Technology, Wright-Patterson Air Force Base, 25 March 1976.

22. "Use of Controlled-Surface-Flaw Technique in the Study of Fracture Behavior in Structural Ceramics," M. G. Mendiratta, presented at the AFWAL/AIAA Mini-Symposium on New Avenues for Progress in Aerospace Research Technology and Systems, Air Force Institute of Technology, Wright-Patterson Air Force Base, 25 March 1976.

23. "Effect of Grain Size upon Flaw and Fracture in a Precipitation-Strengthened Ti-8 wt% Al - 0.25 wt% Si Alloy," M. G. Mendiratta (with S. M. L. Sastry and J. V. Smith), J. Mater. Sci. 11, 1835 (1976).

24. "Controlled-Surface-Flaw-Initiated Fracture in Reaction-Bonded Si_3N_4," M. G. Mendiratta (with R. R. Wills and J. J. Petrovic), J. Mater. Sci. 11, 1330 (1976).

25. "Mixed-Mode Fracture from Controlled Surface Flaws in Hot-Pressed Si_3N_4," M. G. Mendiratta (with J. J. Petrovic), J. Amer. Ceram. Soc. 59, 163 (1976).

26. "Effects of Surface Removal on Fracture from Controlled Surface Flaws," M. G. Mendiratta (with J. J. Petrovic, R. A. Dirks, and L. A. Jacobson), J. Amer. Ceram. Soc. 59, 177 (1976).

27. "Prediction of Fracture-Surface Energy from Microhardness Indentation in Structural Ceramics," M. G. Mendiratta (with J. J. Petrovic), J. Mater. Sci. 11, 973 (1976).

28. "Controlled-Surface-Flaw-Initiated Fracture in Reaction-Densified SiC," R. R. Wills (with J. M. Wimmer), J. Amer. Ceram. Soc. 59, 437 (1976).

29. "Intrinsic Thermal and Mechanical Properties of Reaction-Sintered $Si_4Al_2N_6O_2$ Sialon," R. R. Wills (with J. M. Wimmer and R. W. Stewart), Bull. Amer. Ceram. Soc. 55, 975 (1976).

Section II

FRACTURE FROM CONTROLLED SURFACE FLAWS

INTRODUCTION

In recent years crack patterns produced in the vicinity of microhardness indentations in brittle materials have been the subject of increasing scrutiny.[1-5] In the past such cracking has been viewed as a generally undesirable element associated with the hardness testing of brittle materials; however, it is now recognized that indentation-produced cracks can play a valuable role in determining the fracture behavior of these materials.

One aspect of the use of indentation cracking to investigate brittle fracture is the area of fracture from controlled surface flaws. In this technique surface flaws of controlled size and shape are introduced into a mechanical test specimen by microhardness indentation. Subsequent fracture of the test sample initiates from the site of the controlled surface flaw, and the resultant fracture may be analyzed to derive fracture-mechanics parameters. The present section reviews this method, its applications to date, its advantages and disadvantages, and its potential for future application.

MICROHARDNESS INDENTATION CRACKING

Typical surface crack patterns around microhardness indentations are shown in Figs. 1 and 2, for a diamond-pyramid indentation and a Knoop indentation, respectively. On the surface, sharp cracks radiate from the corners of the diamond-pyramid indentation, while for the Knoop indentation a sharp crack is formed along the long diagonal.

The cracks visible on the surface actually extend below the surface with a semi-elliptical shape, as shown in Fig. 3 for a 2600-gm Knoop indentation in hot-pressed (HP) Si_3N_4. These cracks correspond to the "median vents"

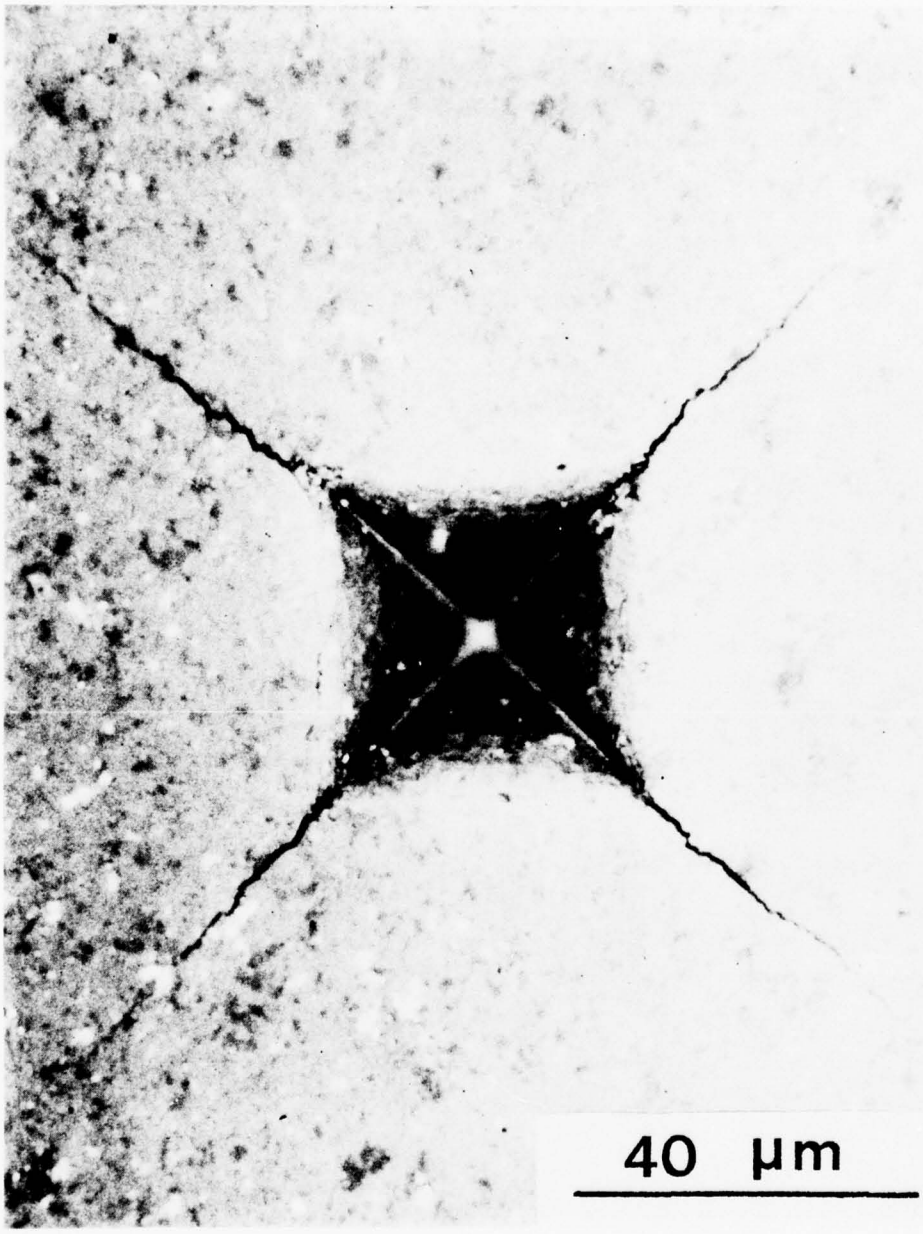

Figure 1. 2600-gm Diamond Pyramid Indentation in HP Si_3N_4
(a) Indentation on Polished Surface

Figure 1. (b) Crack Pattern after 8-µm Surface Removal

Figure 2. 2600-gm Knoop Indentation in HP Si_3N_4
(a) Indentation on Polished Surface

Figure 2. (b) Crack Pattern after 8-µm Surface Removal

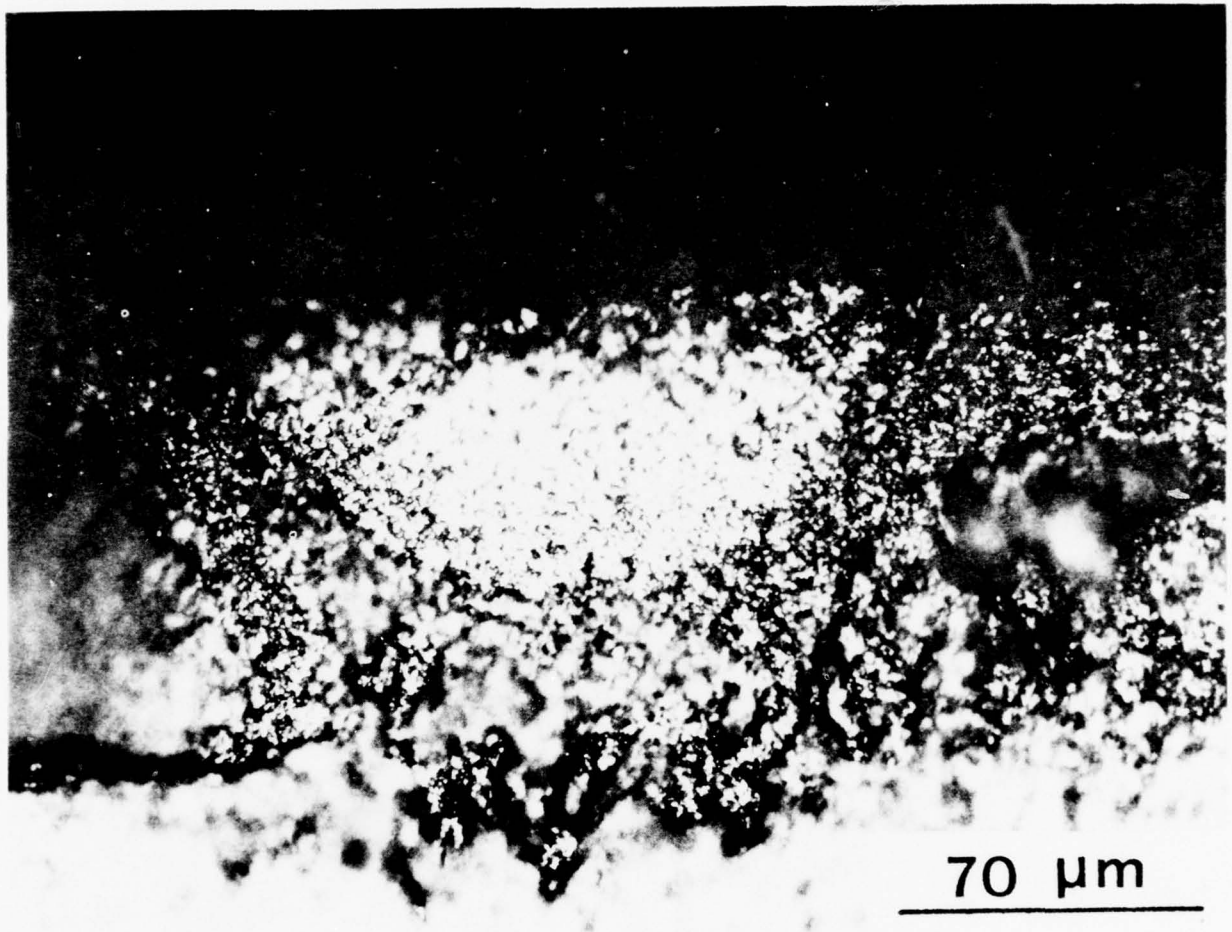

Figure 3. Surface Flaw Produced by a 2600-gm Knoop Indentation in HP Si_3N_4. Flaw profile as seen on a fracture surface.

described by Lawn, et al.[1-3] Thus, with microhardness indentation, it is possible to introduce semi-elliptical surface flaws into brittle materials.

In the present effort, the use of flaws produced by Knoop indentations as opposed to diamond-pyramid indentations was preferred for the following reasons: First, with the Knoop indentation there is no crack perpendicular to the primary surface flaw as there is with the diamond-pyramid indentation. This is a more desirable situation from a fracture-mechanics-analysis point of view. Secondly, orientation of Knoop surface flaws is more convenient and can be controlled more easily since alignment is achieved by aligning the long axis of the Knoop indentation.

Surface flaws produced by Knoop indentation are "controlled" in the sense that their basic shape is semi-elliptical and their size is determined by the applied Knoop microhardness load.

SURFACE FLAWS IN FOUR-POINT BENDING

If a single controlled surface flaw of suitable size is placed on the tensile surface of a four-point bend specimen and accurately aligned perpendicular to the tensile-stress direction, as shown schematically in Fig. 4, fracture initiates at the site of this flaw because it is the "worst flaw" in the specimen. A consequent reduction in fracture stress, as compared to that in the "unflawed" condition, occurs and the surface-flaw profile is visible on the fracture surfaces.

Table I shows the effect of a single surface flaw upon the fracture stress of three structural ceramic materials. Taking Norton HS-130 HP Si_3N_4 as an example, the room-temperature fracture stress of the as-received specimen was 661 MN/m^2. The surface flaw produced by a 2600-gm Knoop indentation was quite small, having a depth (a) of 68.5 μm and a surface length (2c) of 154 μm. For HS-130 Si_3N_4 presence of this flaw reduced the fracture stress to 322 MN/m^2, approximately a factor-of-two reduction. It is also important to notice that the scatter in fracture stress was reduced by a

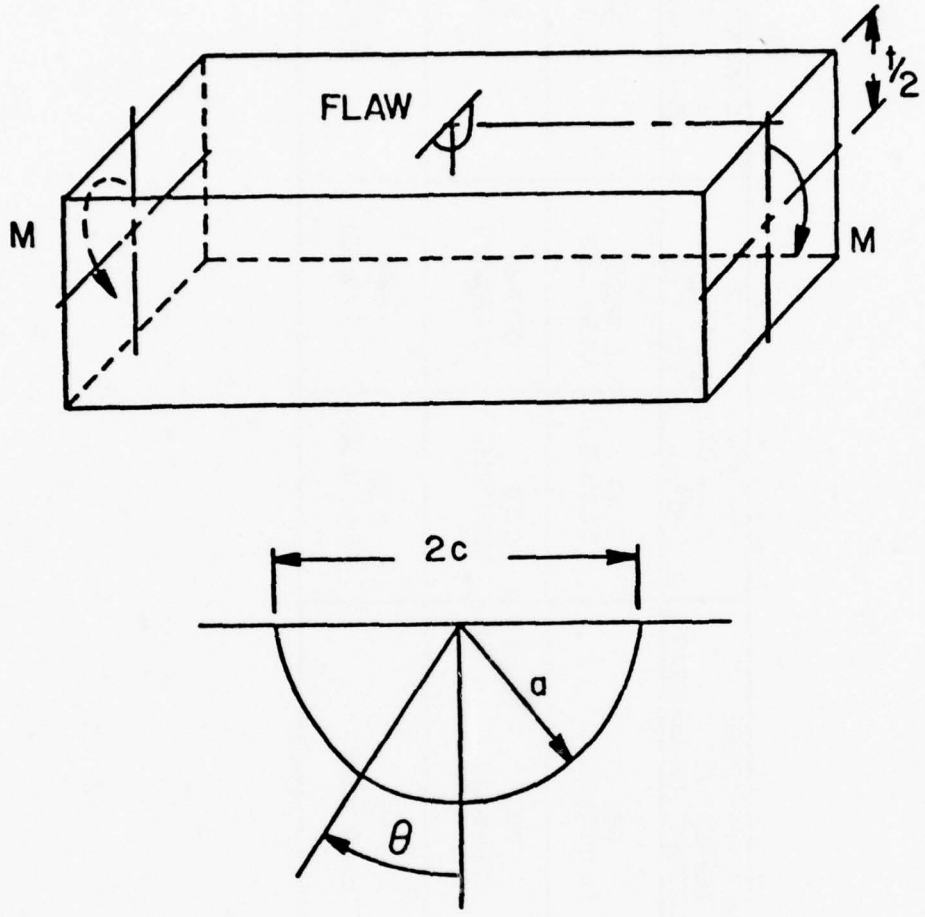

Figure 4. Schematic of Controlled Surface Flaw on the Tensile Surface of a Four-Point Bend Specimen

TABLE I. EFFECT OF ONE CONTROLLED SURFACE FLAW UPON THE FOUR-POINT BEND STRENGTH OF THREE HOT-PRESSED STRUCTURAL CERAMICS

MATERIAL	ROOM TEMPERATURE AS-RECEIVED FRACTURE STRESS (MN/m^2)	2600 GM KNOOP FLAW DIMENSIONS		ROOM TEMPERATURE FLAWED FRACTURE STRESS (MN/m^2)
		$2c$ ($X10^{-3}m$)	a ($X10^{-3}m$)	
HS-130 Si_3N_4	661 (9.48 % SD)	0.154 (7.05 % SD)	0.0685 (3.34% SD)	322 (2.16 % SD)
NC-132 Si_3N_4	614 (14.24 % SD)	0.170 (5.97 % SD)	0.0745 (3.48 % SD)	329 (1.19 % SD)
NC-203 Si C	480 (5.27 % SD)	0.159 (3.49 % SD)	0.0927 (4.27 % SD)	229 (1.35 % SD)

factor of four as a result of the flaw being present. This indicates that the flaws introduced by microhardness indentation were highly reproducible. Similar effects are evident for the other materials in Table I.

FRACTURE MECHANICS OF SURFACE FLAWS

An excellent review of fracture-mechanics expressions for surface and internal cracks has been compiled by Keays.[6] Green and Sneddon[7] and Irwin[8] addressed the question of stresses in the vicinity of an elliptical crack in an infinite medium subjected to tensile loading. The derived stress-intensity factor for the elliptical crack is of the form

$$K_I = \frac{\sigma(\pi a)^{1/2}}{\Phi}\left(\frac{a^2}{c^2}\cos^2\phi + \sin^2\phi\right)^{1/4} \qquad (1)$$

where σ = applied tensile stress, a = minor half-axis, c = major half-axis, and $\phi = \cos^{-1}(x_o/c)$, x_o being a point on the ellipse. The term Φ is given by

$$\Phi = \int_0^{\pi/2}\left[\sin^2\phi + \frac{a^2}{c^2}\cos^2\phi\right]^{1/2} d\phi \qquad (2)$$

The value of Φ increases with the a/c ratio of the elliptical crack, reaching a value of $\Phi = \pi/2$ for a/c = 1. The point of maximum stress intensity occurs at the minor axis of the ellipse where the stress intensity factor is

$$K_I = \frac{\sigma(\pi a)^{1/2}}{\Phi} \qquad (3)$$

If the elliptical crack in the infinite solid is sectioned along its mid-plane, a semi-elliptical surface crack results. Irwin[8] has suggested that the stress-intensity factor for the surface flaw may be described by insertion of a numerical correction factor (M) into Eq. (3); thus,

$$K_I = \frac{\sigma M(\pi a)^{1/2}}{\Phi} \qquad (4)$$

He also developed a plasticity correction factor by adding a yield-zone radius, R_y [$R_y = K_I^2/(4\sqrt{2}\,\pi\sigma_{ys}^2)$], to the crack length in the computation of K_I, which yields

$$K_I = \frac{\sigma M(\pi a)^{1/2}}{\left[\Phi^2 - 0.212\left(\frac{\sigma}{\sigma_{ys}}\right)^2\right]^{1/2}} \tag{5}$$

where σ_{ys} is the tensile yield stress. Thus, the final form of K_I for the surface flaw is

$$K_I = \sigma M\left(\frac{\pi a}{Q}\right)^{1/2} \tag{6}$$

where $Q = \Phi^2 - 0.212(\sigma/\sigma_{ys})^2$.

Although other expressions have been developed for the stress-intensity factor at surface flaws (see Ref. 6), Irwin's simple expression, Eq. (6), is considered to be adequate for small flaws ($a/t < 0.5$, t being specimen thickness) and for situations where plasticity effects are not overriding ($\sigma/\sigma_{ys} < 0.5$). These conditions are usually satisfied for brittle materials.

The numerical correction factor (M) was originally estimated by Irwin[8] to have a value of 1.095. Smith, et al.,[9] indicated that for small, semi-circular surface flaws, the value of M varied from 1.03 at the flaw depth to 1.21 at the surface. Shah and Kobayashi[10] calculated values of M as a function of the a/t ratio and the a/c ratio, observing that M increased as these ratios decreased. Their results yielded M = 1.03 at the flaw depth for small, semicircular flaws. Using a photoelastic-stress freezing and slicing technique, Schroedl and Smith[11] reported good agreement with M values calculated by Shah and Kobayashi for surface flaws.

Equation (6) has been applied to fracture from indentation-produced controlled surface flaws for calculating K_{IC} values. Specimens containing a surface flaw are fractured in four-point bending and the maximum outer-fiber tensile stress determined. Since flaw dimensions can be measured on the fracture

surface, this provides the necessary information to calculate K_{IC} from Eq. (6). For brittle fracture, the plasticity correction term is usually neglected.

CURRENT APPLICATIONS OF THE CONTROLLED-SURFACE-FLAW TECHNIQUE

The controlled-surface-flaw technique has been applied to the measurement of K_{IC} values at both room and elevated temperatures for the structural ceramics Si_3N_4[12-14] and SiC.[15] For the case of SiC, this technique could be used to distinguish differences in fracture behavior associated with air and vacuum environments. Ingelstrom and Nordberg[16] used the method to determine K_{IC} values for WC-Co composite materials at room temperature. Govila[17] has examined the fracture behavior of VC single crystals, measuring fracture-surface energy as a function of temperature.

A slight modification of the technique was employed by Petrovic and Mendiratta in a study of mixed-mode fracture in HP Si_3N_4.[18-19] Rather than orienting the surface flaw perpendicular to the bending-tensile-stress direction, they accurately positioned it at a number of different angles which led to mixed-mode fracture conditions, with Modes I, II, and III being present. This was found to be an experimentally convenient technique for observing mixed-mode fracture.

Mendiratta, Wimmer, and Bransky[20] used the controlled-surface-flaw technique to obtain dynamic K_{IC} values both at room temperature and 1300°C for HP Si_3N_4. Flawed bend bars were employed in conjunction with an instrumented drop-weight apparatus. Dynamic K_{IC} values were less temperature dependent than static K_{IC} values in this material.

The elevated-temperature slow-crack-growth behavior of HP Si_3N_4 was investigated by Mendiratta and Petrovic.[21] In this case arrays of surface flaws of different sizes were placed on a single four-point bend bar and then subjected to stress at elevated temperatures for various time periods. Average crack velocities and K_I values were determined by observation of

surface-crack extension. Slow crack growth from individual flaws was erratic and not well described by the empirical relationship $V = AK_I^n$. Land and Mendiratta[22] have put forward a theoretical framework which explains such behavior in terms of the interactions of the flaw with material inhomogeneities.

It is evident from the above discussion that the controlled-surface-flaw technique has a wide range of applications to date. This technique is useful for examining a number of phenomena associated with the fracture behavior of brittle materials. However, the potential applications for this method have not yet been fully explored.

DISADVANTAGES OF THE CONTROLLED-SURFACE-FLAW TECHNIQUE

As with all fracture-mechanics tests for brittle materials, certain disadvantages are associated with the use of the controlled-surface-flaw method. These are:

1. Residual stress effects
2. Flaw "healing" at elevated temperatures
3. Observation of the flaw profile on the fracture surface
4. Applicability of the technique to a wide range of brittle materials

These advantages will now be discussed in detail.

In order to gather the data shown in Fig. 5, surface flaws were placed on bend bars of HP Si_3N_4; these bars were then subjected to an elevated-temperature air-annealing treatment prior to subsequent fracture at room temperature.[23] Although fracture always initiated at the flaw site, room-temperature K_{IC} values increased as a result of the annealing treatment. This effect was independent of annealing environment since it also occurred for vacuum annealing.[15] Ingelstrom and Nordberg[16] observed similar effects in WC-Co alloys.

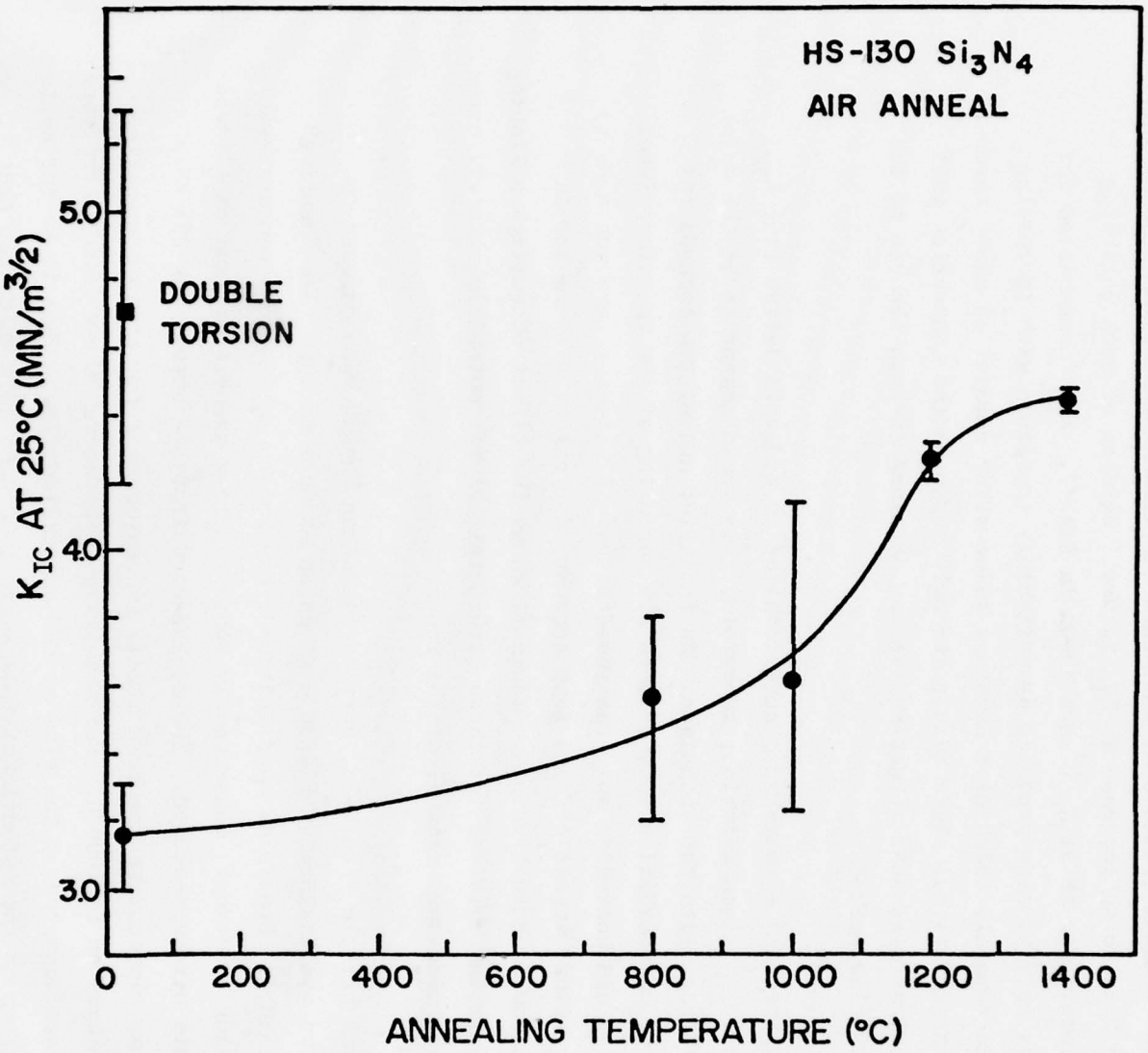

Figure 5. Effect of Annealing on Room-Temperature K_{IC} Values Obtained by the Controlled-Surface-Flaw Technique for HP Si_3N_4

This increase in K_{IC} with annealing has been attributed to a reduction in residual stresses associated with the microhardness indentation used to produce the controlled surface flaw.[12,13,16] If this is the case, then careful surface polishing to remove the indentation zone and associated tensile residual stresses at the crack tip (shown schematically in Fig. 6) should lead to an increase in K_{IC} values. Results of such polishing experiments for HP Si_3N_4 [23] are shown in Fig. 7. K_{IC} (compensated for changes in flaw size produced by polishing) increased with increasing surface removal, reaching a constant value after removal of about three indentation depths. This result strongly supports the contention that residual stresses can affect K_{IC} values obtained through the use of the surface flaw technique.

Residual stress effects must be eliminated in order to derive true K_{IC} values for a given material; therefore, this would appear to be the major disadvantage with the technique. As indicated above, two methods for eliminating residual stress effects are annealing of the indented/flawed material and polishing away the indentation. If attempts are not made to take residual stress effects into account, K_{IC} values will be low in comparison to actual values. Table II shows the effect of surface polishing on K_{IC} values obtained for three structural ceramic materials. In all cases, K_{IC} increased upon removal of the indentation.

For some brittle materials, surface flaws can "heal" when exposed to elevated temperatures. Figure 8 gives an example of such flaw "healing" in HP SiC.[15] Specimens were indented, exposed to an elevated-temperature annealing treatment, subsequently tested at room temperature, and the flawed fracture stress measured. The as-indented fracture stress was 225 MN/m^2. The room-temperature fracture stress increased as a function of annealing temperature up to 1000°C. For annealing temperatures above 1000°C, fracture no longer occurred at the site of the controlled flaw. This is an indication of healing of the intentional flaw above 1000°C to such an extent that it was no longer the worst flaw in the specimen. Note that fracture stresses observed for cases where the flaw had "healed" (1000°C and above) were higher than the strengths for the as-received material, suggesting that flaw-"healing" mechanisms also influenced the nature of surface defects in the as-fabricated samples.

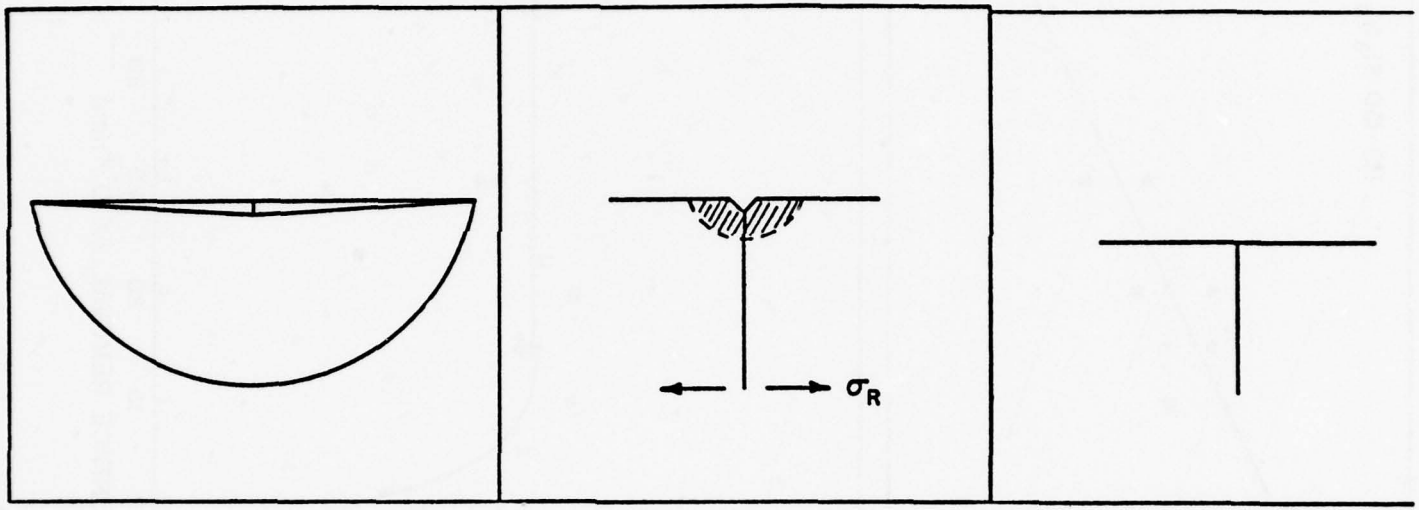

Figure 6. Schematic of Surface Polishing to Remove Residual Stresses Associated with the Microhardness Indentation

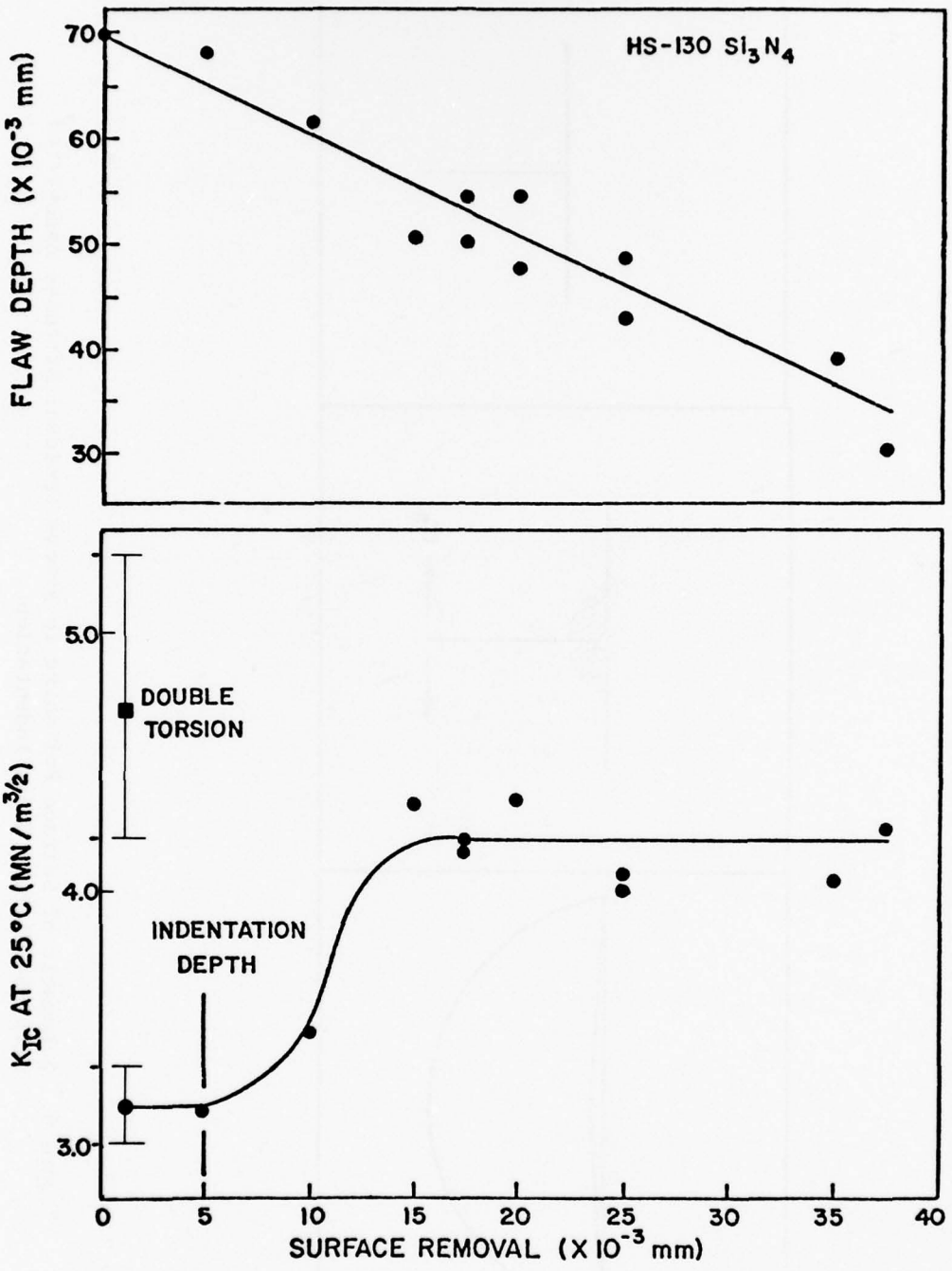

Figure 7. Effect of Surface Polishing on Room-Temperature K_{IC} Values Obtained by the Controlled-Surface-Flaw Technique for HP Si_3N_4

TABLE II. EFFECT OF SURFACE POLISHING UPON ROOM-TEMPERATURE K_{IC} VALUES FOR THREE STRUCTURAL CERAMICS

	K_{IC} AT 25°C ($MN/m^{3/2}$)		
	NC-350 Si_3N_4	HS-130 Si_3N_4	NC-203 SiC
AS-INDENTED	1.15	3.16	2.57
GROUND	1.86	4.20	2.91

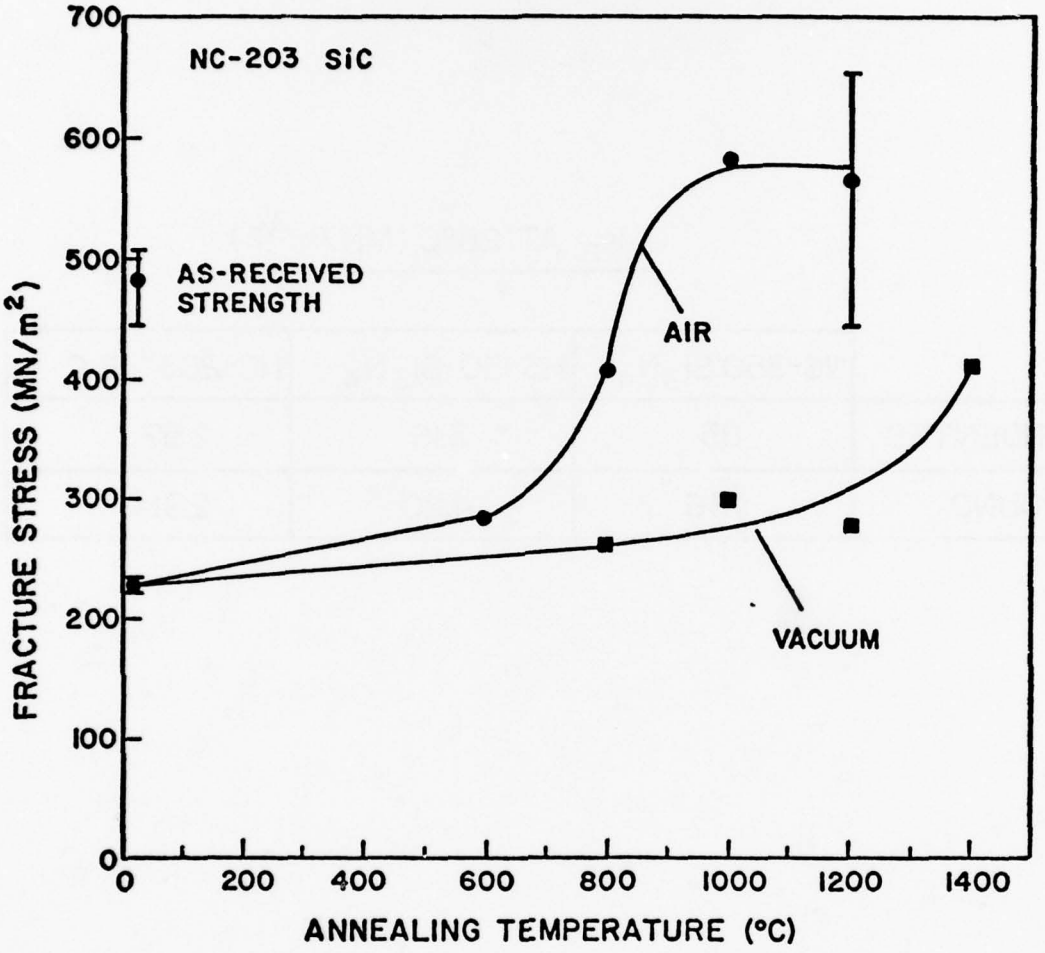

Figure 8. Flawed Fracture Stresses (2600-gm Knoop flaw) of HP SiC at Room Temperature after Elevated-Temperature Annealing

Some flaw healing may have occurred in vacuum, although not to the extent indicated in air (see Fig. 8). This may indicate that part of the healing in the case of SiC was due to relief of residual stresses and part was due to oxidation. For vacuum annealing, the subsequent room-temperature fracture always occurred at the site of the flaw, even for the highest-temperature annealing treatments. For HP SiC the presence of a small preload on the specimen during the air-annealing treatment eliminated the flaw-"healing" effects, a result possibly related to small displacements of the flaw surfaces produced by the preload.

The controlled-surface-flaw technique depends upon the ability to see the flaw profile on the fracture surface. With knowledge of the fracture stress, measured flaw dimensions allow calculation of K_{IC} from Eq. (6). The visibility of the flaw on the fracture surfaces suggests differences between the nature of indentation fracture and subsequent fast, catastrophic fracture from the flaw site. However, the reasons for such differences have not, to the authors' knowledge, been addressed in any definitive way.

Surface-flaw profiles were readily visible on fracture surfaces in HP Si_3N_4[13] and HP SiC.[15] However, flaws were somewhat more difficult to observe in reaction-sintered (RS) Si_3N_4[14] which is a material having large porosity. This suggests the possibility that in some brittle materials, flaws may be essentially invisible on fracture surfaces. In this case, laborious but definitive incremental polishing techniques could be employed to establish the flaw-profile dimensions.[13] A systematic study of surface-flaw visibility over a wide range of brittle materials has not been performed.

An appropriate question is whether semi-elliptical surface flaws of reproducible sizes can be introduced into all brittle materials using microhardness indentation. For example, if grain-size and density limits to the production of these flaws exist, the size and shape of flaws could become ill-defined and nonreproducible. It seems likely that such limits exist, but their range has not yet been defined.

ADVANTAGES OF THE CONTROLLED-SURFACE-FLAW TECHNIQUE

The controlled-surface-flaw method has distinct advantages with regard to examination of fracture in brittle materials. Foremost among these are:

1. A simple bend-bar specimen geometry is used.
2. Potential exists for adaptation of the technique to other specimen geometries.
3. The controlled surface flaw approximates natural failure defects in brittle materials.

Applications of the controlled-surface-flaw technique to date have employed a four-point bend-bar test specimen which is small, inexpensive, and can be obtained readily in most situations. Furthermore, bend tests are experimentally convenient to perform. For these reasons, controlled-surface-flaw experiments can be conducted under severe environmental conditions such as high temperatures, controlled atmospheres, corrosive environments, and high strain rates. Thus, the controlled-surface-flaw technique possesses a high degree of versatility with regard to potential applications.

Controlled surface flaws have potential for use with specimen geometries other than the bend bar. A controlled surface flaw might be placed on the surface of a disc specimen and the disc fractured in biaxial flexure.[24] Often in brittle-materials development programs, only small quantities of material are produced. In such instances bend bars may not always be available, although right cylinders can usually be made. With a right cylinder, the diametral-compression test[25] could be used in conjunction with a properly oriented controlled surface flaw on the flat end of the cylinder (where tensile stresses exist) to fracture the material in tension using a compressive loading mode and thus derive values of K_{IC}.

An interesting question arises with regard to the use of controlled surface flaws in conjunction with the direct compression test: Will the controlled surface flaw which is the "worst flaw" in tension also be the "worst flaw"

in compression? If not, then this would constitute a significant observation in itself. However, if so, controlled surface flaws might be used to examine details of compressive fracture. Such flaws could be placed, suitably inclined, on the circumferential surface of a right-cylindrical compression specimen and thus be subjected to compressive loading.

Surface flaws could also be loaded in torsion. In such cases, fracture would be a combination of Modes II and III, with no Mode I being present. It may also be possible to investigate mixed-mode fracture using combinations of tension/torsion and compression/torsion.

Controlled surface flaws approximate actual failure defects in brittle materials, with fracture initiating from a very small crack which is well characterized in terms of its size and shape. Although this crack is the "worst flaw" in the material, its size is still close to the size range of naturally occurring material defects.

The following question should be addressed: Are small flaws equivalent to large cracks with respect to the fracture of brittle materials? It seems possible that small flaws interact more directly with local material inhomogeneities such as porosity, grain boundaries, and compositional variations to produce differences in fracture behavior related to the size of the fracture-initiating crack. Recent studies[21,22] have indicated that this may be true with respect to elevated-temperature slow crack growth.

CONCLUSIONS

Controlled surface flaws associated with microhardness indentations can be a valuable tool in the examination of various aspects of brittle fracture. In this method semi-elliptical surface flaws of controlled size and shape produced by Knoop indentation initiate fracture in four-point bend specimens. Fracture-mechanics analysis for surface flaws in bending may be applied to this fracture to obtain the critical stress-intensity factor K_{IC}. The technique, which employs a simple specimen geometry and is experimentally convenient, has been used to derive both static and dynamic K_{IC} values at

both ambient and elevated temperatures as well as to examine mixed-mode fracture and elevated-temperature slow crack growth. Effects of residual stresses associated with the microhardness indentation required to produce the controlled surface flaw constitute the major disadvantage of the technique. Its advantages include simplicity and versatility; in addition, the fracture-initiating crack approximates natural defects in brittle materials.

Section III

FRACTOGRAPHIC STUDIES ON REACTION-SINTERED Si_3N_4

INTRODUCTION

Reaction-sintered silicon nitride (RS Si_3N_4) has emerged as a leading candidate material for Air Force systems applications such as gas-turbine stators,[26] missile heat shields and nozzles,[27] radomes, and other applications such as bearings and furnace components. This material is an attractive choice for such applications because it can be easily and economically fabricated into near-net complex shapes by either pressing or slip casting silicon powder and subsequently nitriding the green compacts. In addition, RS Si_3N_4 exhibits excellent thermal shock, oxidation, corrosion, and erosion resistance and has reasonably high strength at room temperature with good strength retention up to 1400°C; no measurable subcritical crack growth has been detected up to 1400°C.

An extensive property screening and evaluation of RS Si_3N_4 is currently being carried out by IIT Research Institute (IITRI), Chicago, under the sponsorship of the Air Force Materials Laboratory (Contract F33615-75-C-5196). One of the properties being measured is the four-point-bend tensile fracture strength, σ_f, as a function of testing temperature. Since there is no measurable plasticity in RS Si_3N_4, even at very high temperature, strength variations can be directly interpreted on the basis of fracture-mechanics considerations involving the size of the critical flaw and the intrinsic materials parameters which are fracture-surface energy, γ, and Young's Modulus, E. The strength-controlling flaws are introduced by the particular processing and fabrication procedures and machining utilized in RS Si_3N_4 obtained from different suppliers; the identification and characterization of these flaws is of extreme importance in understanding the fracture-strength variation as related to processing and fabrication. Fractographic examination by scanning electron microscopy (SEM) is emerging as a powerful technique in achieving this understanding in structural ceramics.

The objective of the present study was to perform a comprehensive fractographic investigation on RS Si_3N_4 bars fractured in four-point bending by IITRI at room temperature and at 1200, 1350, and 1500°C. IITRI has carried out strength measurements and other property evaluation on ceramics supplied by two different suppliers--Norton RS Si_3N_4 (NC-350 Si_3N_4) and Kawecki-Berylco RS Si_3N_4 (KBI Si_3N_4). Both materials were included in the present fractography study. The objective of this study was to gain an understanding of the fracture behavior and also establish fracture-mechanics parameters (i.e., relationship between flaw size, fracture mirror size, and strength) to aid in the failure analysis of structural components made from RS Si_3N_4.

MATERIALS STUDIED AND EXPERIMENTAL PROCEDURE

The Norton NC-350 RS Si_3N_4 used in this study was prepared by cold pressing a large silicon plate which was then nitrided. Samples were diamond machined to a surface finish of ~ 5 μm RMS. The KBI RS Si_3N_4 samples were machined from a cold-pressed silicon block, individually nitrided, and then finished by diamond machining. Surface finish ranged from 20 to 60 μm RMS. Impurity analysis of both materials has been presented previously;[28] in general, the Norton material has a somewhat higher purity. In light of the above differences in the two materials, different microstructural features may govern the fracture behavior. Similar materials from two different suppliers were studied in the hope that a better understanding of the features chat control fracture could be gained. The four-point bend strength, elastic modulus, and density of the two materials have been measured and included in the IITRI report.[28]

The bend bars fractured at different temperatures were obtained from IITRI. All pieces were inspected under a 14-60× binocular light microscope in order to look for the characteristic radiating ridges which are often observed to converge toward the origin of the fracture and frequently to originate in a smooth, sometimes mirror-like region surrounding the flaw. At room temperature the bars generally broke into two or three pieces, and the localized critical flaws could usually be identified with confidence from the fracture markings. However, at high temperatures the bars broke in

many pieces, and identification of the primary fracture surface and, therefore, the location of the critical flaw was difficult due to missing pieces, damage to the primary feature area, and occurrence of flaws and mirrors at secondary fracture sites with dimensions comparable to those at primary sites. The pieces containing probable critical flaws and several examples of secondary fractures were designated for study in the SEM.

While making observations with the light microscope, the pieces of broken bar were reassembled in order to determine the position of the critical flaw and to permit tracing of the fracture features. Pieces of the bars were selected for study and photographing in an AMR SEM. These pieces were coated with a thin uniform inner layer of carbon and a thicker outer layer of gold-palladium alloy which is the combination giving the best SEM signal and resolution. The SEM examination was usually performed in the secondary-emission mode which is particularly suitable for observing gross three-dimensional features in fracture topography. The backscattered electron mode was also employed selectively; in this mode the high-energy reflected electrons travel in more nearly straight lines and, therefore, the finer topographic features of the fracture are emphasized by shadows in the image.

RESULTS AND DISCUSSION

Fracture Modes and Fracture Microstructures

Fracture surfaces of both the NC-350 Si_3N_4 and KBI Si_3N_4 bend bars were examined in the SEM for general fracture features. Representative examples of fracture surfaces for specimens broken at room temperature are shown in the SEM micrographs in Fig. 9 for NC-350 and in Fig. 10 (a) and (b) for KBI Si_3N_4. As shown in Fig. 9, the fracture surface of NC-350 exhibited uniform, planar features representing the transgranular fracture mode. These planar features representing grains were measured to be ~ 3-6 μm. A relatively uniform distribution of pores having a size range of 1.5-2 μm can be observed from the micrograph; however, isolated larger pores or pore-coagglomerates having a size of ~ 10 μm were also observed frequently (shown at locations A

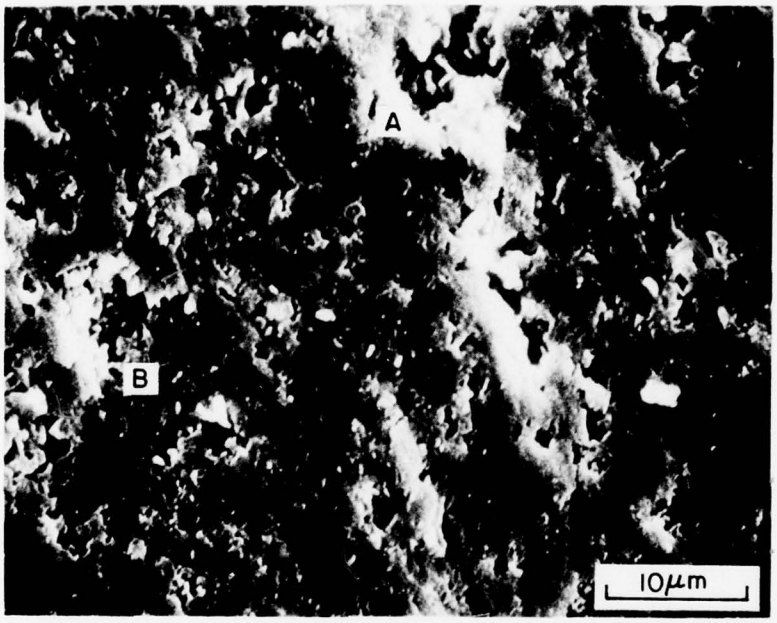

Figure 9. Fracture Surface Showing Microstructure of NC-350 Si_3N_4. Bend Bar Fractured at room temperature. Secondary-electron SEM micrograph.

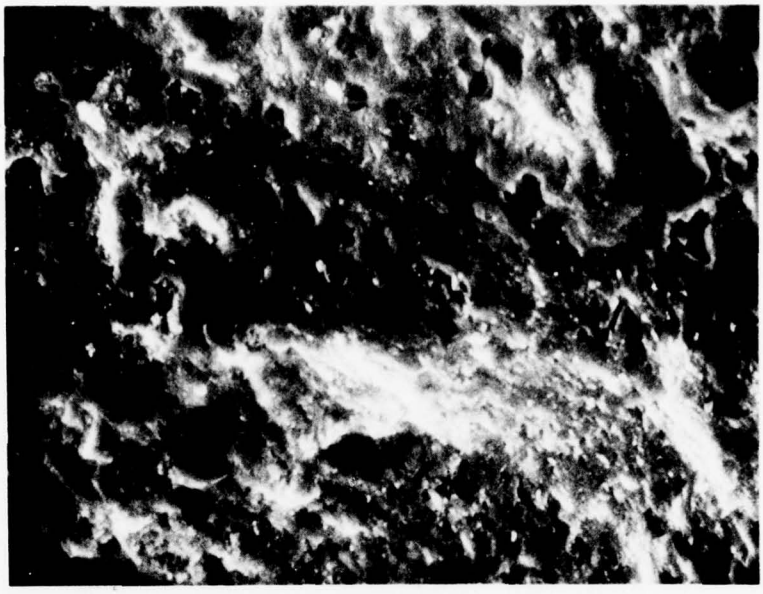

(a)

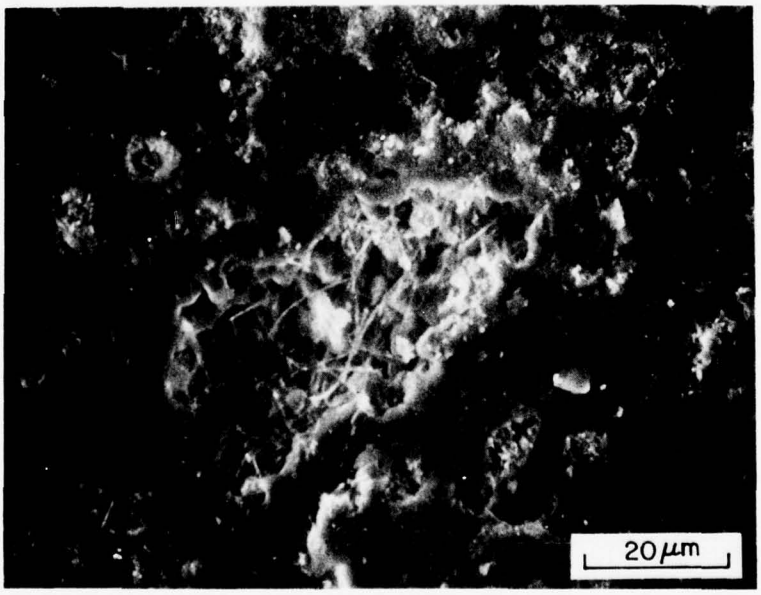

(b)

Figure 10. Fracture Surfaces Showing Microstructure of KBI Si_3N_4. Bend bar fractured at room temperature.

and B in Fig. 9). The volume fraction of the porosity was measured by standard lineal analysis and had a value of ~ 20%. This value is in reasonable agreement with that estimated from the measured density.[28]

In contrast to the relatively sharp fracture features in NC-350, for the KBI material, in general, diffused nonuniform fracture features were revealed [see Fig. 10 (a) and (b)]. Figure 10 (a) shows ill-defined features giving a wooly appearance; it is difficult to determine whether the fracture is transgranular or intergranular. Small pores having a size range of ~ 2-5 μm can be seen in the micrograph. Many large pores showing unreacted material and having a size of ~ 50 μm were also observed frequently; an example of such a pore can be seen in Fig. 10 (b).

The fracture features for the two materials as described above were observed some distance away from the fracture-originating flaws. These general features were common to most of the bend bars and, therefore, independent of strength distribution. The more uniform fracture features, the flat transgranular fracture mode, and the smaller, more uniform porosity in the NC-350 material indicate that this material had been more completely sintered than the KBI material. For this reason, NC-350 should exhibit less scatter in strength values and a higher mean strength value than that exhibited by the KBI material. The strength data given in the IITRI report[28] indicate that indeed such is the case.

The more undefined and rough features in the fracture surfaces of the KBI bend bars (Fig. 11) indicate that a higher fracture-surface energy may have been expended in propagating the cracks than that in the NC-350 bend bars (Fig. 9). The fracture-surface-energy values calculated from room-temperature K_{IC} data are 15.8 J/m^2 for the KBI material and 11.3 J/m^2 for the NC-350 material.[28] These values and the fracture appearance for the two materials are consistent.

High-Temperature Fracture Appearance

Detailed fractography for high temperature was carried out only for NC-350 Si_3N_4, the reason being that NC-350 Si_3N_4 exhibited consistently higher

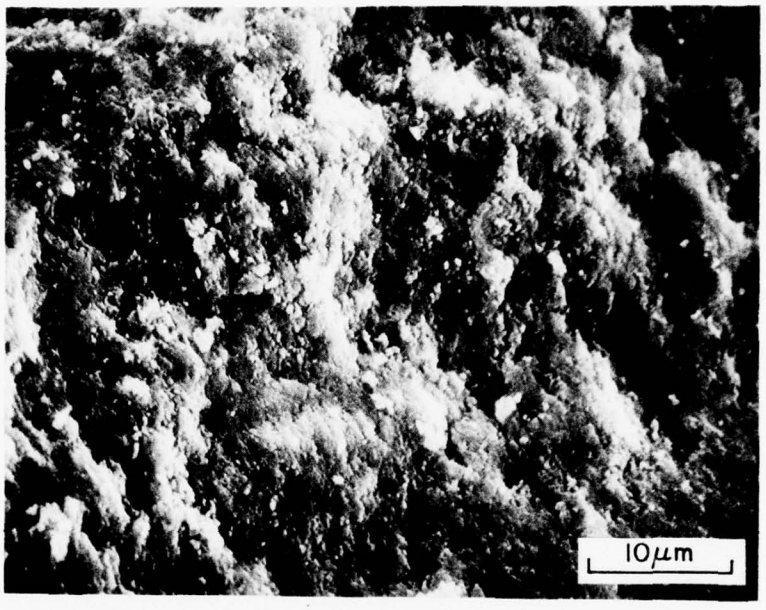

Figure 11. Fracture Surface Showing Microstructure of NC-350 Si_3N_4 Fractured at 1200°C in Air. Secondary-electron SEM micrograph.

strength than KBI Si_3N_4. The strength at 1200°C in air increased significantly as compared to that at room temperature; above 1200°C the strength dropped slightly but still was higher than that at room temperature. It was hoped that fractography of the bend bars broken at elevated temperatures might give a clue as to the reasons for the increase in strength levels at elevated temperatures.

The fracture surfaces of bend bars broken at 1200°C exhibited a marked difference in appearance as compared to those broken at room temperature. The 1200°C fracture surface did not show uniform, planar features; rather it showed diffused, undefined features similar to the room-temperature fracture exhibited by KBI material. Figure 11 is an SEM micrograph of the fracture surface of a bend bar broken at 1200°C in air. From the appearance it is difficult to judge whether the fracture mode is transgranular or intergranular; however, in comparison with the room-temperature fracture appearance, the fracture mode has definitely changed.

In order to determine whether oxidation of the fracture surface at 1200°C would obscure the fracture features, two bend bars were broken at the Air Force Materials Laboratory in four-point loading in a vacuum of 10^{-4} torr. The fracture-strength values are given in Table III.

TABLE III. FOUR-POINT FLEXURAL STRENGTH AT 1200°C FOR NC-350 Si_3N_4

Test Atmosphere	Average Strength
Air	65 ksi (IITRI data)
Vacuum	34 ksi

The fracture-surface appearance of the bend bars broken at 1200°C in vacuum was very similar to that of the bars broken at 1200°C in air (Fig. 11). Oxidation at 1200°C, therefore, did not obscure the appearance of the fracture surfaces, and it can be stated that there was a definite change in fracture mode at high temperatures as compared to room temperature. However, this change did not seem to affect the strength values; an average strength value of 34 ksi at 1200°C in vacuum was obtained which is very near the average value at room temperature. The strength increase at 1200°C in air could possibly be due to flaw-tip blunting by the formation of a thin layer of silica and the consequent increase in effective fracture-surface energy, γ. The short pretest time at 1200°C is not expected to decrease the critical-flaw sizes significantly but could blunt sharp flaws.

Fracture Origins

The sites of fracture origins were located by searching for inner mirrors bounded by rough radiating ridges in the fracture surfaces of the bend bars. The preliminary search for mirrors was made on the binocular light microscope and in the SEM at magnifications below 20×. The fracture-originating flaws were then observed at successively higher magnifications in the SEM. Only in ~ 40% of the bend bars could the fracture mirrors be seen; in the remainder of the fractured bars, either the regions containing the mirrors were chipped away due to multiple fracture or the mechanisms that produce clearly observable mirrors were not operative; e.g., for large flaws and low fracture strength, the crack-growth velocity may be too low for the formation of mirror boundaries.[29]

In both NC-350 and KBI Si_3N_4, the most dominant fracture-originating flaws observed following the above procedure were pores and pore agglomerates. However, a number of other types of flaws were also observed. These were:

1. Bands of porosity (pores 10-20 μm in diam.)
2. Bands of glassy-looking phase, perhaps indicating local overheating of the material during the fabrication procedure or local chemistry differences

3. Machining flaws, i.e., surface chipping and surface gouging. Only about 10% of the fracture surfaces observed indicated that machining flaws were fracture initiating. It appears that machining damage is insignificant in RS Si_3N_4.
4. Flaked, fibrous band of material, signifying incomplete local nitriding.

Except for machining flaws, the other types of flaws described above are obviously the result of the impurities and size distribution of silicon powders used and the nitriding and sintering procedures. Since the materials were obtained from commercial sources, it was not possible in the present study to relate the nature of the flaws observed by SEM to the fabrication procedures. Attempts were made to obtain chemistry variations in the immediate vicinity of some of the flaws utilizing the energy-dispersive x-ray technique; however, no significant differences in chemistry could be detected.

Fracture Mirrors

Clearly delineated fracture mirrors could be observed only in the NC-350 Si_3N_4. In the KBI material, although vague impressions of a mirror region were observed, it was difficult to measure--even approximately--the size of the inner mirror. Figures 12, 13, and 14 are SEM micrographs showing mirrors and fracture-originating flaws at room temperature and at 1200 and 1500°C for NC-350 Si_3N_4. The flaws in these examples are pores and unsintered material representing material inhomogeneity and are not caused by machining.

In NC-350 attempts were made to measure mirror sizes and to establish a correlation between flaw mirror sizes and between mirror size and strength. In most cases it was difficult to establish the boundaries of the inner, flat, highly reflecting regions (i.e., inner mirrors); it appeared that very fine radiating ridges began forming close to the critical flaws. The measured mirror sizes were very approximate and--independent of testing temperature--had a value of 120 ± 20 μm. The reason for the mirror

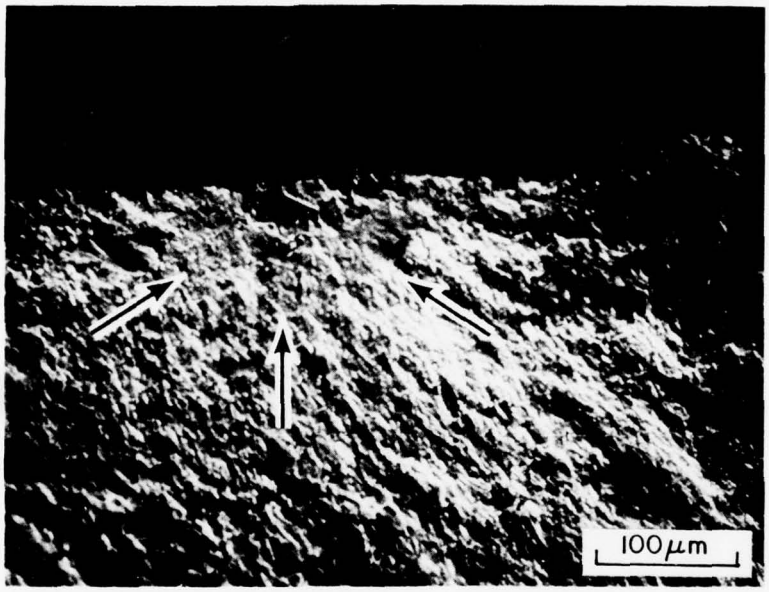

Figure 12. Fracture-Originating Flaw and Associated Inner Mirror in NC-350 Si_3N_4. Room-temperature fracture. Inner mirror shown by arrows.

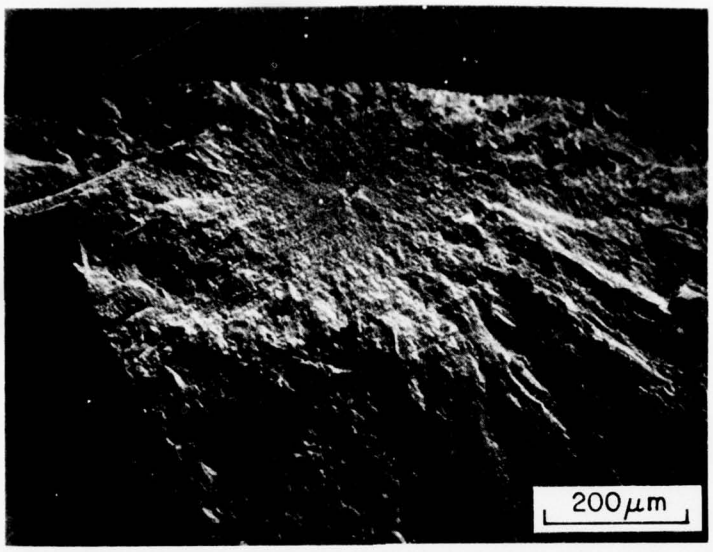

(a)

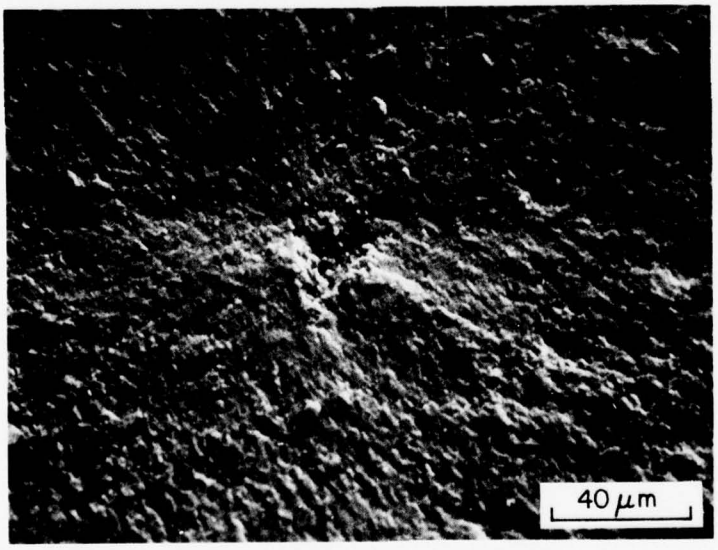

(b)

Figure 13. Fracture-Originating Flaw in NC-350 Si_3N_4 Bend Bar Fractured at 1200°C in Air. (a) and (b) are in B.S. mode; (c) is in S.E. mode.

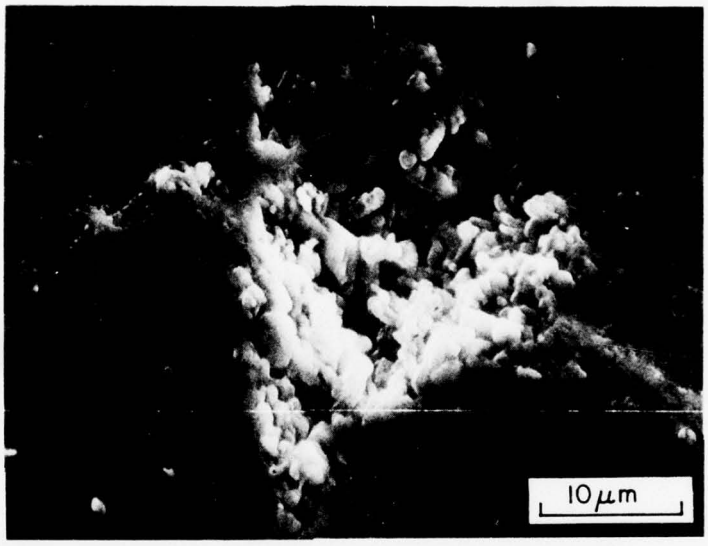

(c)

Figure 13 (cont'd)

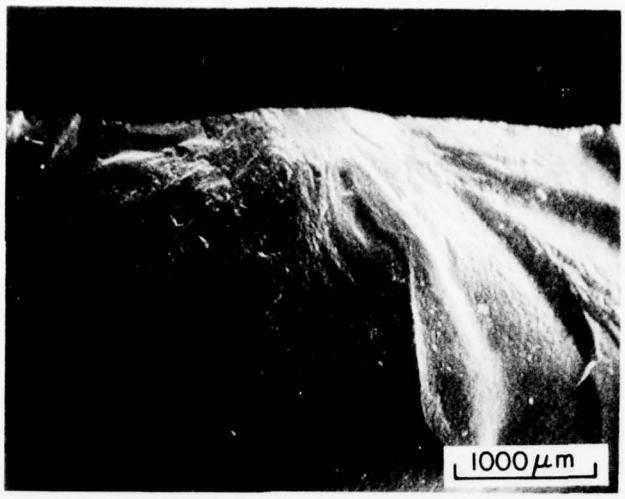

(a)

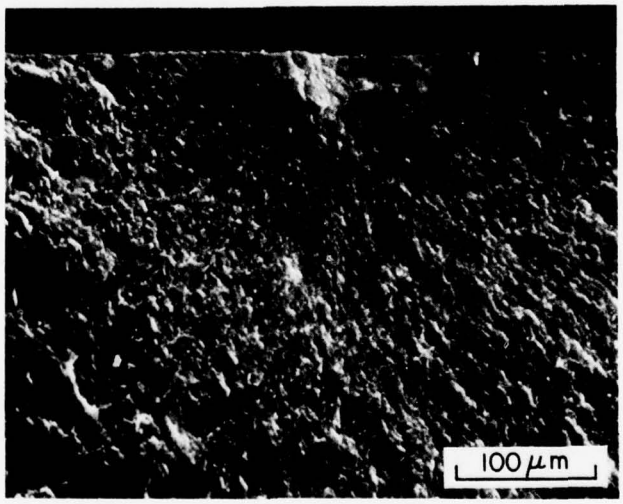

(b)

Figure 14. Fracture-Originating Flaw in NC-350 Si_3N_4 Bend Bar Fractured at 1500°C in Air (S.E. Mode)

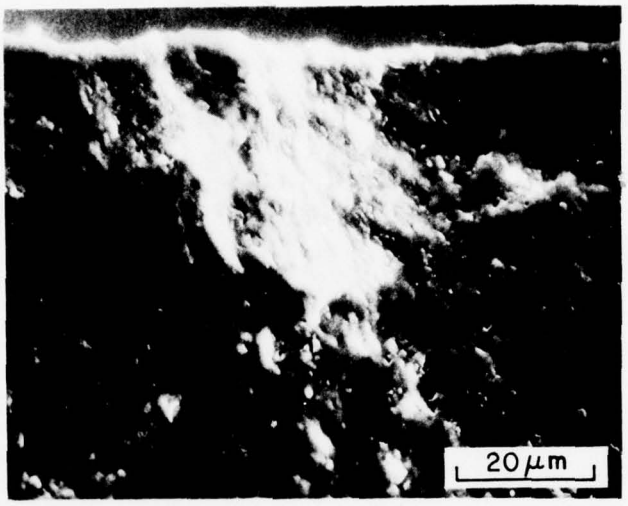

(c)

Figure 14 (cont'd)

boundaries not being sharply delineated is not known. The associated critical flaw sizes had a mean value of 25 ± 5 μm, providing a ratio of inner mirror to flaw size of ~ 5. It has been shown that for many glasses and ceramics, the strength and size of the mirror are related by

$$\sigma_f \sqrt{R} = \text{a constant (for a given material)}$$

where σ_f is fracture strength and R is the mirror radius. For NC-350 the mean value of this parameter was found to be 2.6 $MN/m^{3/2}$ with a variation of as much as ± 30%. The major uncertainty in the calculation of this parameter was due to ambiguity in establishing precisely the inner mirror boundaries.

K_{IC} Calculations

Attempts were made to calculate approximately the critical stress-intensity factor, K_{IC}, from fracture-strength values and measured flaw dimensions. The flaws were assumed to be circular flat discs in the depth of bend bars, and in this case the stress-intensity factor is given by[30]

$$K_{IC} = \frac{2}{\sqrt{\pi}} \sigma_f (a)^{1/2}$$

where σ is the tensile stress and a is the radius of the circular flaw. In the depth of the bend bars, the local value of σ was calculated by assuming a linear variation of the stress with depth, with maximum value at the surface and zero at the center of the bar, i.e., at the neutral axis. For the flaws which were open to the surface or very near the surface, K_{IC} was calculated from the more precise expression[6]

$$K_{IC} = M\sigma_f \left(\frac{\pi a}{Q}\right)^{1/2}$$

where M is a function of the ratios of flaw depth to bend bar thickness and flaw depth to flaw length and Q is a function of ellipticity, i.e., the ratio of flaw depth to flaw length.

For NC-350 Si_3N_4 the room-temperature values of K_{IC} were found to vary between 1.22 and 1.6 $MN/m^{3/2}$. The double-torsion technique was utilized by IITRI to obtain a room-temperature K_{IC} value for NC-350; a mean value of 2.06 MN/m^2 was reported. This value is somewhat higher than the values calculated in the present investigation. This difference may be due to highly local stress intensification and weak material in the vicinity of small material flaws in contrast to the large artificial crack utilized in the double-torsion technique which averages the microstructural variations. It is interesting to note that average K_{IC} values of 1.87 $MN/m^{3/2}$ were obtained by Wills, et al.,[31] who utilized a controlled-surface-flaw technique; in this technique a surface flaw having a depth of ~ 135 μm was utilized. This crack dimension is about four times larger than the dimensions of the natural critical flaws but is much smaller than the crack front size used in double torsion.

At elevated temperatures, although the strength in air increased substantially, the dimensions of the critical flaws were not different than those at room temperature, i.e., ~ 25 μm. The calculated values of K_{IC} were found to be 2.1 to 2.4 $MN/m^{3/2}$ at high temperatures (i.e., above 1200°C), with no systematic dependence upon temperature. The increase in K_{IC} at higher temperatures was probably due to increased fracture-surface energy resulting from flaw-tip blunting.

SUMMARY

A fractographic study was carried out on two reaction-bonded silicon nitride materials--Norton NC-350 Si_3N_4 and KBI Si_3N_4 by SEM. The fracture surfaces of the bars fractured in four-point bending at room temperature and at 1200, 1350, and 1500°C were examined. In bars tested at room temperature, the general fracture features in NC-350 Si_3N_4 were uniform, planar features representing the transgranular fracture mode, uniformly distributed small pores having a size range of 1-2 μm or less, and isolated large pores having a size of ~ 10 μm. In contrast, the KBI material tested at room temperature exhibited nonuniform, diffuse, and ill-defined fracture features, small pores having a size range of 2-5 μm, and many large pores having a size of

~ 50 μm. In some regions the KBI material exhibited features similar to those in NC-350 Si_3N_4, i.e., transgranular and uniform, which indicated that the KBI material did not have a uniform microstructure, probably due to inadequate reaction bonding. The room-temperature strength variations, i.e., higher mean strength and less scatter in strength values in the NC-350 material than in the KBI material, are consistent with the differences in general fracture features in the two materials. At high temperatures the fracture appearance in NC-350 Si_3N_4 was ill defined and diffuse, indicating a change in fracture mode. However, this change in mode in itself did not seem to increase the fracture-surface energy.

In NC-350 fracture mirrors were frequently observed, although the boundaries of inner mirrors were ill defined. The fracture-originating flaws in NC-350 were predominantly the large pores or pore agglomerates, although other types of flaws--including bands of small pores, bands of a glassy-looking phase, surface chipping and gauging, and a flaked and fibrous band of material--were present. In the KBI material, because of diffuse and ill-defined fracture features, it was not possible to observe mirrors and, therefore, the sites of fracture initiation.

In NC-350 the measured radius of the inner mirrors had a mean value of 120 ± 20 μm and the size of the associated critical flaw had a mean value of 25 ± 5 μm, thus providing a ratio of the inner mirror to flaw size of ~ 5. The parameter $\sigma_f \sqrt{R}$ had a value of 2.6 $MN/m^{3/2}$ with a variation of as much as ± 30%. Thus, in the failure analysis of a component where it may be possible to measure the radius of the inner mirror, the local stress could be predicted to within ± 30%. At room temperature the values of K_{IC} ranged from 1.22 to 1.6 $MN/m^{3/2}$. At high temperatures, the calculated K_{IC} values were between 2.1 and 2.4 $MN/m^{3/2}$.

Section IV

OXIDATION BEHAVIOR OF TITANIUM ALUMINIDES

Most of the fundamental research on the oxidation behavior of titanium aluminides has been reported in Ref. 32. Significant results from additional fundamental studies in this area are summarized below.

EFFECT OF TEMPERATURE UPON THE OXIDATION BEHAVIOR OF TITANIUM ALUMINIDES

Figure 15 shows the parabolic rate constants for oxidation of TiAl and Ti_3Al in air and oxygen as functions of temperature. The k_p values for Ti_3Al oxidation indicate predominantly TiO_2-forming kinetics, and the rate constants are not influenced by the oxidizing atmosphere (viz., oxygen or air).

The k_p values for oxidation of TiAl in air or oxygen above 1050°C are not significantly different and are indicative of TiO_2-forming kinetics. At lower temperatures the k_p values for oxidation in air deviate somewhat from the TiO_2-forming kinetics; however, the overall rates are still much higher than those characteristic of alumina-forming kinetics. For the oxidation of TiAl in oxygen at or below 950°C, the k_p values indicate alumina-forming kinetics. For 1050°C oxidation in O_2, time-dependent k_p values were exhibited, k_p being low at the beginning of an experiment and monotonically approaching the high value with time. Thus, the transition from titania- to alumina-forming kinetics for oxidation in O_2 begins at 1050°C and is essentially complete at 950°C.

MICROSTRUCTURAL CHARACTERIZATION OF THE OXIDE SCALES

Scale Morphology for TiAl

The oxide-scale morphologies for oxidation of TiAl in air have been described previously.[32] The scale morphologies for oxidation in oxygen above 1000°C

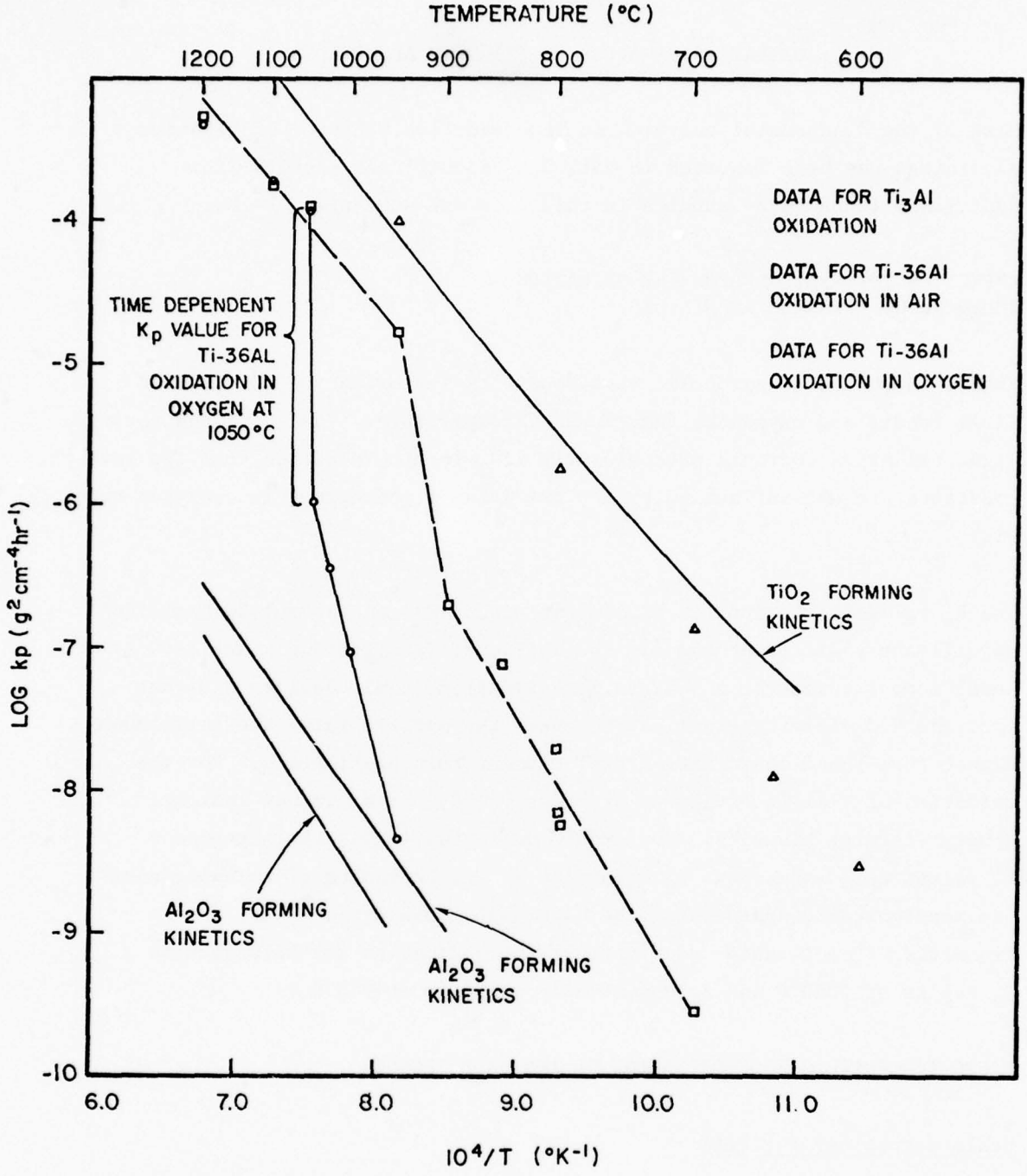

Figure 15. Plot of log k_p as a Function of 1/T Showing Data Obtained for Oxidation of Ti-36 w/o Al in Air and in O_2

are similar to those in air. The oxide scale is characterized by an outer TiO_2 layer, beneath which is a mixed-oxide layer composed of titania and alumina. A metallic layer is also formed between the substrate and the oxide. This metallic layer has been identified by TEM to have a Ti_3Al-type crystal structure.

Figure 16 is a backscattered electron image and elemental distribution patterns of a transverse section of a TiAl alloy oxidized in air at 1000°C. The elemental distribution patterns corroborate the findings that the outer oxide layer is mainly titania and the inner oxide layer is a mixed oxide of titania and alumina. Figure 17 shows electron-probe line scans across the Ti_3Al layer formed in the same sample. The Ti and O concentration increases in the Ti_3Al layer (as compared to the TiAl matrix), and the Al concentration decreases.

At temperatures above 1050°C, an internal-oxidation zone (restricted within the Ti_3Al layer) is observed. Figure 18 is a backscattered electron image and elemental distribution patterns of the internal-oxidation zone for a TiAl sample oxidized in air at 1200°C. This figure shows that the internal oxide is deficient in Ti, indicating that the internal oxide is probably alumina.

The scale formed upon oxidation of TiAl in oxygen at or below 950°C is grayish and extremely adherent and is composed of a thin layer of alumina with little or no trace of titania. The absence of a Ti_3Al layer between the scale and the substrate is noteworthy.

Scale Morphology for Ti_3Al

Figure 19 is a photomicrograph of a transverse section of a Ti_3Al alloy oxidized in air at 950°C. A qualitative similarity in the oxide-scale morphologies for oxidation of TiAl and Ti_3Al is discernible. The outer oxide layer is mainly titania (the relative thickness of this layer being much greater than that for TiAl oxidation); beneath this layer is a mixed titania and alumina layer.

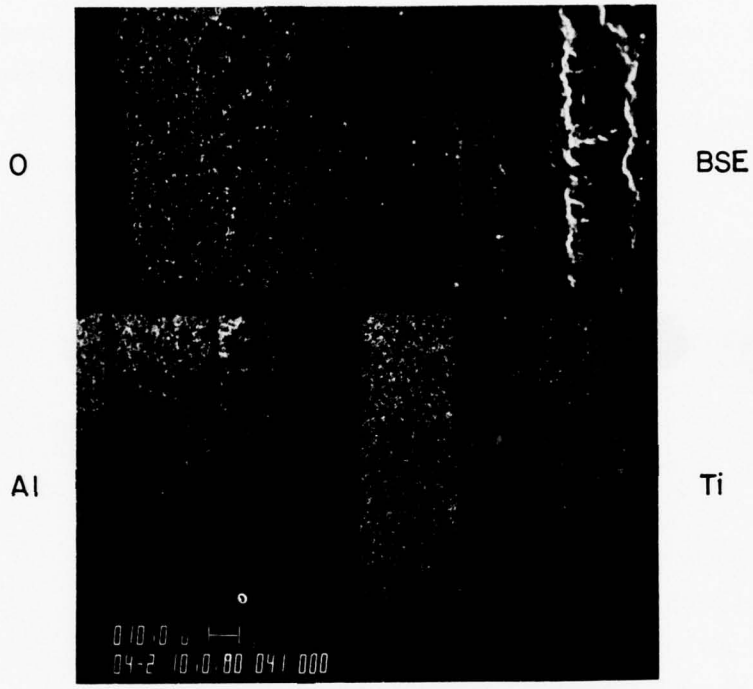

Figure 16. Backscattered Electron Image and Elemental Distribution Patterns of a Transverse Section of a Ti-36 Al Alloy Oxidized in Air at 1000°C

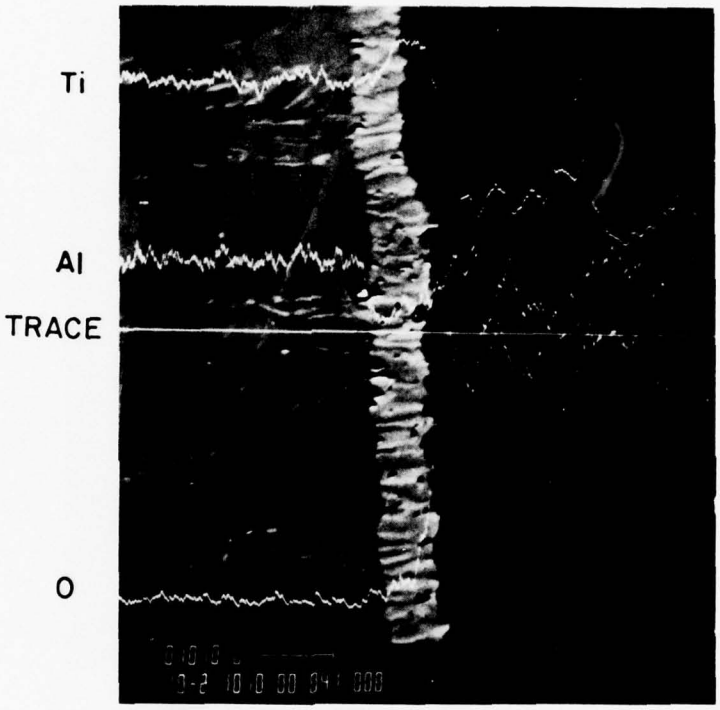

Figure 17. Electron Microprobe Line Scans through a Transverse Section of Ti-36Al Alloy Oxidized in Air at 1000°C

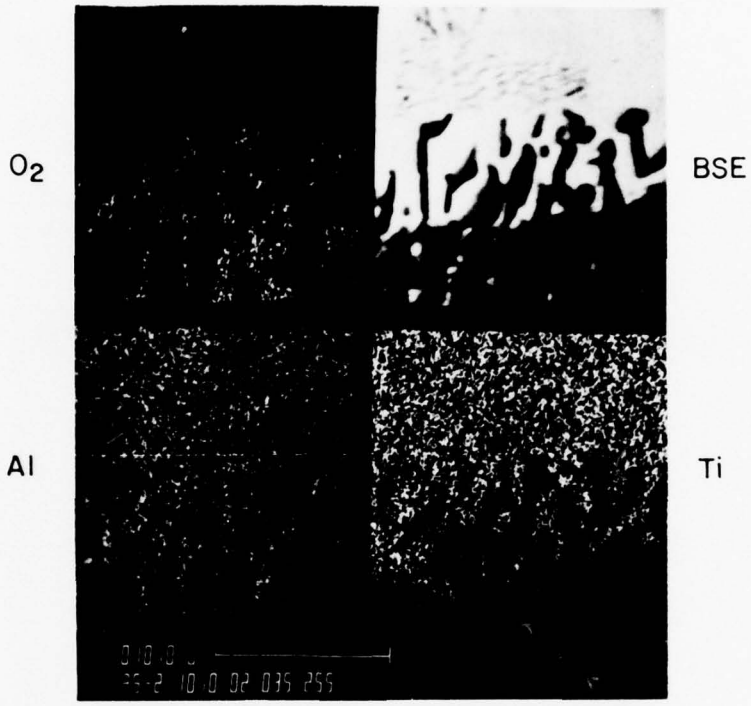

Figure 18. Backscattered Electron Image and Elemental Distribution Patterns of a Ti-36 Al Alloy Oxidized in Air at 1200°C

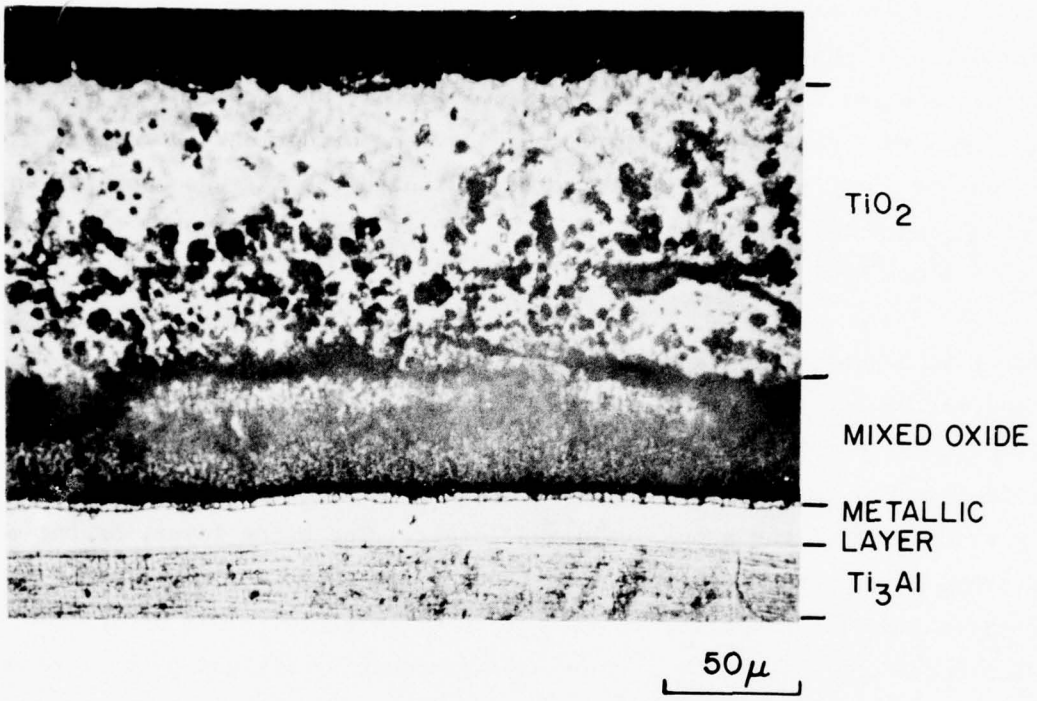

Figure 19. Photomicrograph of a Transverse Section of a Ti_3Al Alloy Oxidized in Air at 950°C

Figure 20 shows electron-probe line scans across the inner metallic layer formed during oxidation in the same specimen. The Al and Ti concentrations in this layer are about the same as those in the matrix, but there is a slight increase in the O concentration. TEM investigations on the metallic layer formed upon oxidation of Ti_3Al have indicated that this layer is disordered, i.e., the crystal structure is similar to α-Ti. The growth of the disordered metallic layer is probably due to diffusion of N or O in this metallic phase. In order to observe the effect of nitrogen, a sample was exposed to a mixture of 50% N_2, 49.8% CO, and 0.2% CO_2 at 950°C. It was hoped that the CO/CO_2 mixture would prevent oxidation. However, oxidation could not be entirely prevented, although the rate was considerably reduced--k_p in this mixture was 3.75×10^{-7} $g^2cm^{-4}hr^{-1}$ as compared to $k_p \approx 10^{-5}$ $g^2cm^{-4}hr^{-1}$ for oxidation in air.

Figure 21 is a photomicrograph of a transverse section of the sample oxidized for 25 hr. In comparing Figs. 21 and 19 (which is for oxidation at 950°C in air for 5.6 hr), it can be noted that the thickness of the metallic layer of the sample oxidized in the N_2, CO/CO_2 mixture is approximately twice that of the sample oxidized in air. The oxide layer, on the other hand, is approximately ten times thicker for oxidation in air as compared to that for oxidation in the N_2, CO/CO_2 mixture. This indicates that the formation and growth of the layer proceeds by diffusion of nitrogen and/or oxygen to the alloy rather than by diffusion of Ti and Al to the oxide.

In Ref. 32, the role of N_2 in promoting titania-forming kinetics for oxidation of TiAl is discussed and a mechanism to explain the effect proposed. In the proposed mechanism, it was assumed that N_2 diffusing through the scale (grain-boundary diffusion) stabilizes the Ti_3Al (α_2) layer. The aluminum activity at the α_2/scale interface is thereby lowered, resulting in predominantly TiO_2-forming kinetics. As oxidation proceeds, the growth of the α_2 phase is controlled, on the one hand, by the oxidation of α_2 at the α_2/scale interface and, on the other hand, by the rate-determining flux of either Al arriving from the alloy/α_2 interface and becoming oxidized at the scale/α_2 interface or the flux of N_2 arriving

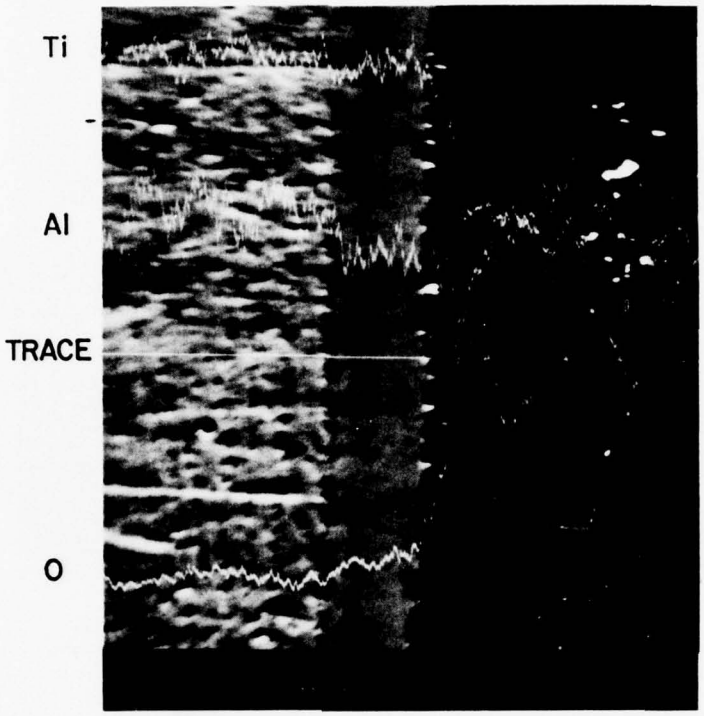

Figure 20. Electron Microprobe Line Scans of a Ti_3Al Alloy Oxidized in Air at 950°C

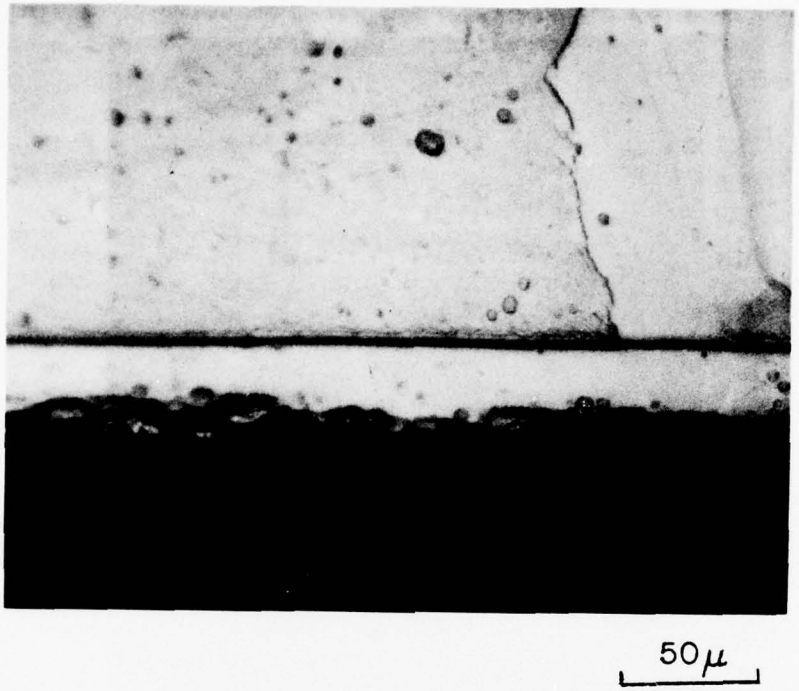

Figure 21. Photomicrograph of a Transverse Section of a Ti_3Al Sample Oxidized at 950°C in a 50% N_2, 49.8% CO, 0.2% CO_2 Mixture

from the scale/α_2 interface and proceeding to the α_2/alloy interface. At temperatures above 1050°C, O_2 also stabilizes the α_2-layer, and the role of O_2 is similar to that of N_2.

In the oxidation of TiAl in air, only one metallic layer (viz., the α_2-layer) is observed between the scale and the matrix. However, in the oxidation of Ti_3Al, the metallic layer formed between the scale and the matrix is disordered, i.e., the crystal structure is that of α-Ti. The absence of an α-Ti layer atop the α_2-layer formed during oxidation of TiAl requires some explanation. It is possible that during the oxidation of TiAl, the flux of Al through the α_2-layer is sufficiently large to allow the aluminum chemical potential at the scale/α_2 interface to be effectively maintained at a higher level than that necessary for α-Ti, $\alpha_2(Ti_3Al)$ coexistence; thus, no α-Ti layer forms on the $\alpha_2(Ti_3Al)$ layer.

EFFECT OF COMPOSITION UPON THE OXIDATION BEHAVIOR OF BINARY TiAl ALLOYS IN AIR AT 950°C

In order to determine whether increased Al content in TiAl alloys promotes Al_2O_3-forming kinetics, two alloys--Ti-38.7 w/o Al (665) and Ti-40 w/o Al (5102)--were oxidized in air at 950°C. The observed k_p values for these alloys were 2.67×10^{-6} and 1.85×10^{-6} $g^2cm^{-4}hr^{-1}$, respectively--well within the scatter range of k_p values observed for oxidation of Ti-36 w/o Al (i.e., TiAl) alloys in air at 950°C. Thus, it is apparent that increasing the Al content from 36 to 40 w/o had no appreciable effect upon the oxidation behavior in air at 950°C.

RESULTS OF OXIDATION TESTS OF ALLOYS BASED UPON TiAl AND Ti_3Al

A number of alloys based upon TiAl and Ti_3Al were subjected to cyclic and noncyclic oxidation tests in order to evaluate the relative oxidation resistances of these alloys. The results are tabulated in Tables IV and V. The beneficial effect of Nb and W additions is worth noting. This effect is probably due to increased Al activity in these ternary and quaternary alloys, which promotes relatively more Al_2O_3 (as compared to TiO_2) formation and reduces k_p and increases scale adherence.

TABLE IV. SUMMARY OF OXIDATION TESTS ON TiAl-BASE ALLOYS IN AIR

MATERIAL	TEMPERATURE (°C)	LOG K_p	TIME (HR)	COMMENTS
Ti-36Al (6169)	950	-5.8	24	
Ti-36Al-2.5Nb (6172)	950	-6.16	25	
Ti-36Al-5Nb (6171)	950	-7.40	24	Alloy - Solution treated at 1150°C for 2 hr then aged at 950°C for 8 hr
Ti-36Al-5Nb (6170-4)	950	-7.37	24	Alloy - As extruded
Ti-36Al-5Nb (6170-8)	950	-7.61	72	Alloy - Aged at 950°C for 8 hr
Ti-36Al-5Nb (6171)	850	-8.19	137	
Ti-36Al-5Nb (6171)	850	-8.18	118	Cyclic Test - No spalling
Ti-36Al-5Nb (6171)	900	-7.61	144	Cyclic Test - No spalling; however, visual observation of the oxidized scale indicates formation of TiO_2 islands on the surface.
Ti-32.5Al-4.6Nb-5W (6632)	950	-7.30	100	
Ti-32.5Al-4.6Nb-5W (6632)	900	-7.65	144	Cyclic Test - No spalling
Ti-32.5Al-4.6Nb-5W (6632)	950	-7.04	70	Cyclic Test - Spalls after 68 hr
Ti-35.1Al-1.4Cr (796) (as forged)	950	-4.88	13	K_p value larger than Ti-36Al
Ti-34.1Al-4.1Cr (797) (as forged)	950	-5.20	24	K_p value larger than Ti-36Al
Ti-32.3Al-9.77W	950	-7.41	26	
Ti-32.3Al-9.77W	950	-7.51	149	Cyclic Test - No spalling
Ti-32.3Al-9.77W	950	-7.29	164	Cyclic Test - Slight spalling noticed after removing the sample
Ti-32.3Al-9.77W	1000	-6.85	24	
Ti-32.3Al-9.77W	1000	-6.77	47	Cyclic Test - Spalling after 25 hr
Ti-32.3Al-9.77W	1050	-6.23	20	
Ti-32.3Al-9.77W	1050	-6.30	28	Cyclic Test - Spalling noticed after start of cycle

TABLE V. SUMMARY OF OXIDATION TESTS OF Ti_3Al-BASE ALLOYS IN AIR

MATERIAL	TEMPERATURE (°C)	LOG K_p	TIME (HR)	COMMENTS
Ti-16Al (6116)	700	-8.51	144	Cyclic - No Spalling
Ti-16Al (6116)	750	-7.65 (up to 72 hr)	144	Cyclic - Spalling After 72 hr
Ti-16Al (6116)	800	-7.07	92	Noncyclic - But Scale Cracks During Run
Ti-16Al-5Nb (6120)	750	-8.34	144	Cyclic - No Spalling
Ti-16Al-5Nb (6120)	800	-8.10	122	Noncyclic
Ti-16Al-5Nb (6120)	800	-8.10	144	Cyclic - Spalling
Ti-16Al-10Nb (6430)	800	-8.13	144	Cyclic - No Spalling
Ti-16Al-10Nb (6430)	850	-7.74	144	Cyclic - Spalling
Ti-14.6Al-10Nb-4W (6629-1)	850	-7.70	196	Cyclic - No Spalling
Ti-14.6Al-10Nb-4W (6629-1)	900	-7.03	144	Cyclic - No Spalling
Ti-14.6Al-10Nb-4W (6629-1)	950	-6.59	40	Cyclic - Spalling
Ti-13.2Al-21.5Nb (6914) (Ti-24 a/o Al-11 a/o Nb)	900	-7.54	50	Noncyclic
Ti-13.2Al-21.5Nb (6914)	950	-7.33	48	Noncyclic
Ti-13.2Al-21.5Nb (6914)	950	-6.96	162	Cyclic - No Spalling; However, Visual Exam. of Sample After Run Indicates Early Signs of Spalling

Section V

STEADY-STATE CREEP BEHAVIOR OF Ti_3Al-BASE INTERMETALLICS

INTRODUCTION

Considerable research efforts are presently being directed toward development of α_2-phase titanium aluminides as structural materials for aircraft turbine engines. The α_2-phase is based upon the composition Ti_3Al and has an ordered DO_{19}-type lattice structure. Recent work[33] has shown that the Ti_3Al-base alloys--although brittle at low temperatures--retain reasonable strength levels up to 800°C. At about 550°C the alloys begin to exhibit measurable ductility which increases gradually with increasing temperature. The tensile deformation modes in Ti_3Al have been studied by Williams and Blackburn at room temperature[34] and by Sastry and Lipsitt at 700°C.[35] The main findings of these investigations are that slip in Ti_3Al is highly planar and is comprised mostly of $\frac{a}{6}\langle 11\bar{2}0\rangle$-type ("a") dislocations. A few $\frac{a}{6}\langle 11\bar{2}6\rangle$-type ("c+a") dislocations have also been observed.[34] The ordered lattice structure and restriction of slip systems observed in Ti_3Al appear to be responsible for both the high-temperature strength and the low-temperature brittleness. Ordering-transformations[35] and strain-amplitude-controlled cyclic deformation[36] studies have also been carried out recently on Ti_3Al-base intermetallics.

The present investigation is directed toward an understanding of the steady-state creep behavior in Ti_3Al-base materials in the stress and temperature ranges which correspond to practical applications. This goal was pursued by establishing the stress and temperature dependences of the steady-state creep rates and examining the creep dislocation substructures by transmission electron microscopy (TEM).

EXPERIMENTAL PROCEDURE

Two intermetallics were used in this investigation: the near-stoichiometric Ti_3Al (nominal composition: Ti-16 w/o Nb) and Ti_3Al + 10 w/o Nb (nominal composition: Ti-16 w/o Al-10 w/o Nb). Nb is added in the Ti_3Al-base alloy primarily to improve the oxidation resistance; significant improvement has been shown to occur[37] with the addition of 5 - 10 w/o Nb. The alloy used in this study was cast as rod ingots and converted by Nuclear Metals, Inc., to a powder form of -35 mesh using a rotating electrode process. The powders were packed in Ti-6Al-4V cans, evacuated, sealed, and hot extruded at 1200°C with an extrusion ratio of 26:1. The details of the extrusion process, the method of specimen machining, and the geometry of the specimen are described in a recent paper.[38] The machined specimens were given an annealing treatment of 1000°C/4 hr in vacuum in order to stabilize the microstructure and were then furnace cooled.

A lever-type constant-load creep machine was utilized for the creep experiments. The tests were performed in air at stresses ranging from 69 to 312 MN/m^2 (10-45 ksi) and at temperatures ranging from 550 to 825°C. During the creep tests the temperature was controlled to within ± 2°C. Most of the tests were carried out at constant (nominal) stresses; however, in some tests stress levels were increased on the same specimen after the onset of steady-state creep. In all experiments the steady-state creep regimes were observed to be well established below 2% total strain. Thus, the correction necessary to convert the nominal stress to true stress was very small and, therefore, neglected. In the creep experiments the specimen elongation was continuously recorded by means of an LVDT and a mechanical

extensometer clamped onto the flanges of the specimens. After the creep had proceeded well into the steady-state regimes, creep tests were discontinued and specimens cooled under load to minimize recovery of the deformation structures. Thin foils for TEM examination were prepared from crept specimens utilizing standard procedures.[39]

RESULTS AND DISCUSSION

Microstructures of the Heat-Treated Intermetallics

The microstructures of the extruded and subsequently heat-treated Ti_3Al and Ti_3Al + 10 Nb are shown in the light micrographs of Fig. 22 (a) and (b), respectively. For Ti_3Al the heat treatment produced a nearly equiaxed grain structure (average grain size ~ 100 μm) with some jagged grain boundaries. For Ti_3Al + 10 Nb the microstructure consisted of highly irregular (i.e., nonequiaxed) grains having very jagged boundaries. Also in Ti_3Al + 10 Nb the average grain size was smaller (~ 60 μm) than that in Ti_3Al. It appears that Nb additions in Ti_3Al retard the diffusive processes required for recrystallization and grain growth. Polished specimens of both intermetallics were scanned in the electron microprobe over distances up to 1 mm; the characteristic x-ray intensities corresponding to Ti, Al, and Nb did not exhibit compositional heterogeneities. TEM bright-field and selected-area-diffraction examination of thin foils revealed the presence of only the ordered α_2-phase in both the Ti_3Al and Ti_3Al + 10 Nb. In Ti_3Al the grains contained a very low density of dislocations and were uniformly recovered. In Ti_3Al + 10 Nb, however, while some of the grains were observed to be nearly fully recovered, most of them consisted of aligned rather thin long subgrains. Most

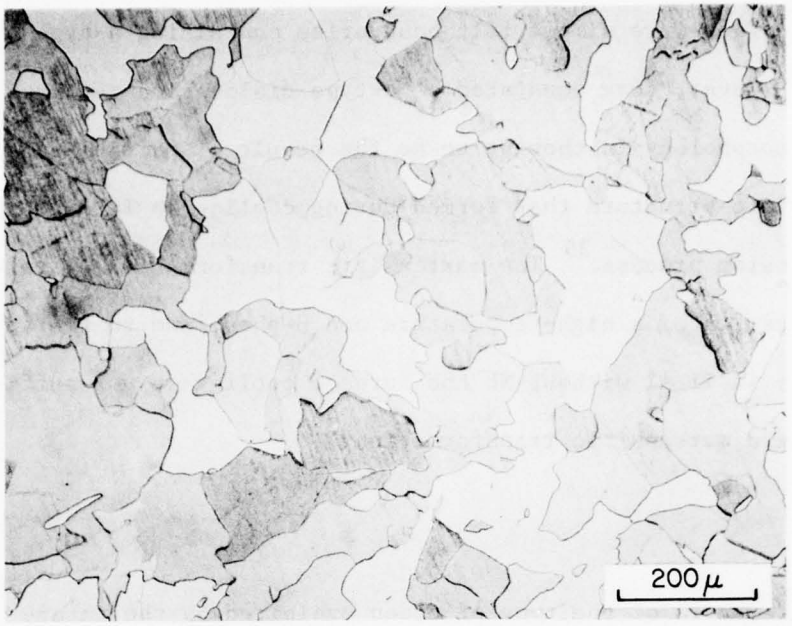

Figure 22(a). Microstructure of Extruded and Heat-Treated Ti-16Al. Extrusion is followed by 1000°C/4 hr → furnace cool.

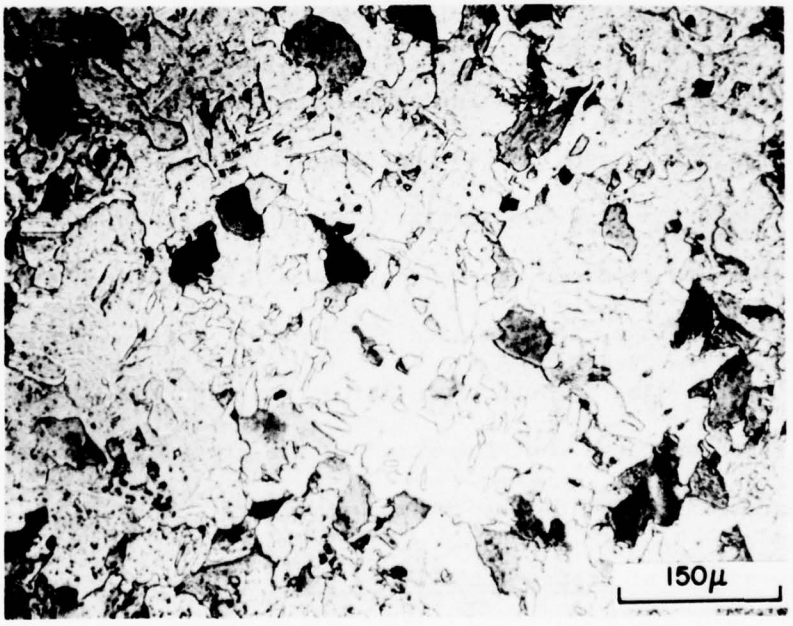

Figure 22(b). Light Micrograph Showing Microstructure of Extruded and Heat-Treated Ti_3Al + 10 wt% Nb. Heat treatment 1000°C/ 4 hr → air cool.

of the subboundaries were simple tilt boundaries containing a-type dislocations; however, some consisted of a-type dislocation networks. The long-subgrain morphology is thought to be the result of partial annealing of the martensitic structure that formed during cooling in Ti_3Al + 10 Nb after the extrusion process.[35] The martensitic transformation is related to the stabilization of a high-temperature bcc β-phase due to the addition of Nb in Ti_3Al; in Ti_3Al without Nb the furnace cooling is not sufficiently fast to produce a martensitic transformation.[35]

Creep Curves

Figure 23 is an example of the type of creep exhibited by the intermetallics. At all stresses and temperatures utilized, the creep curves exhibited primary regimes followed by steady-state creep. In the stress-change experiments in which the stress was increased after the establishment of the steady-state creep regime, further creep was again exhibited. These observations indicated that in the intermetallics used in this investigation, the creep deformation proceeds by the continued formation of a more creep-resistant substructure during the primary stage and by stabilization of this structure by some recovery process(es) during the steady-state stage. For the same stress values, the measured steady-state creep rates were found to be about the same in both the single-stress and the stress-change experiments. This indicated that the steady-state creep was not sensitive to the differences in the prior deformation structure.

Temperature Dependence of Steady-State Creep Rate

Ti_3Al. Steady-state creep rates, $\dot{\varepsilon}_s$, were obtained by calculating the slopes of the secondary regimes of the types of creep curves shown in Fig. 23.

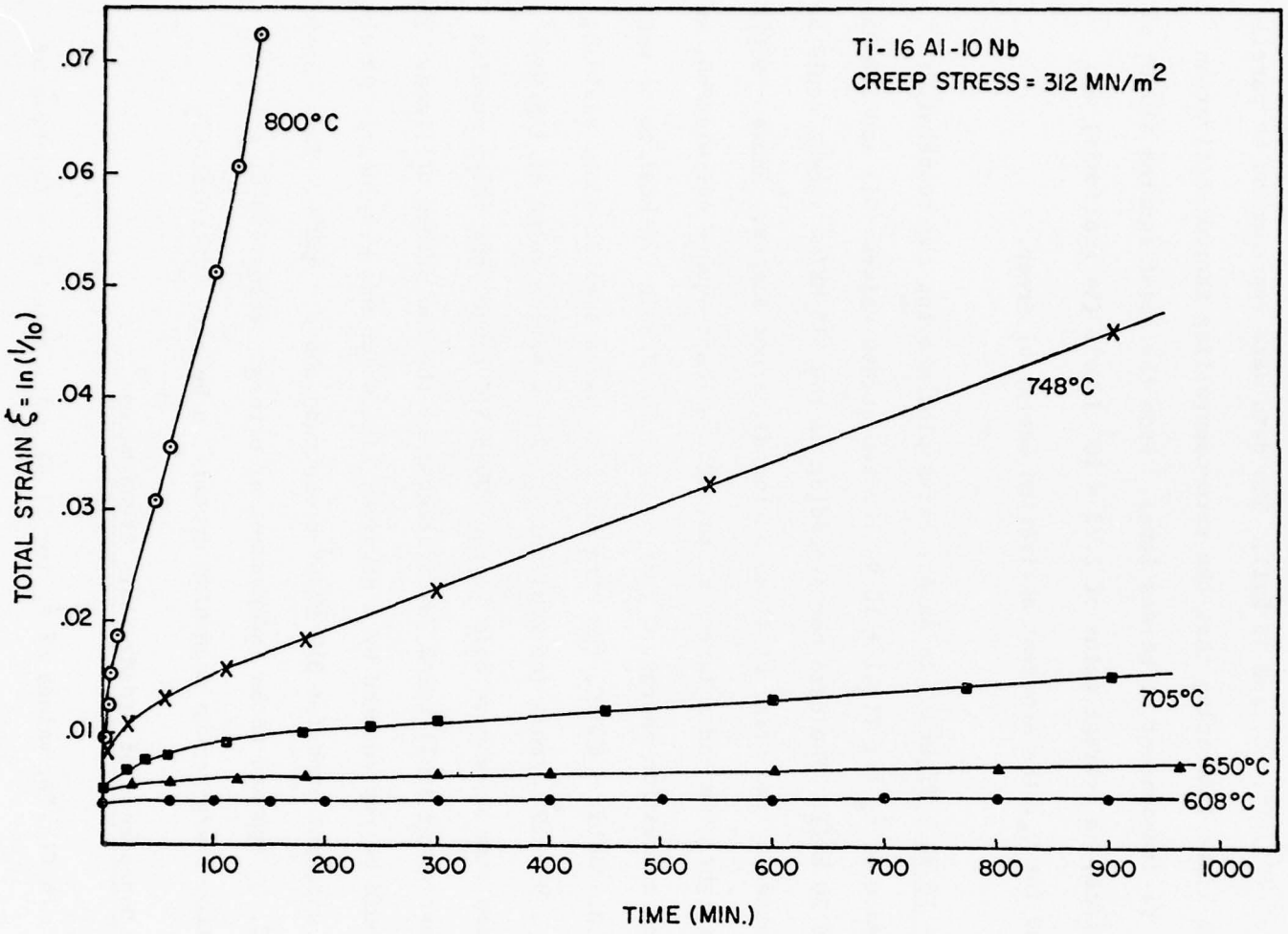

Figure 23. Creep Curves for Ti_3Al + 10 wt% Nb

For Ti_3Al $\dot{\varepsilon}_s$ is plotted in Fig. 24 as a function of the reciprocal of the absolute temperature, 1/T, for four stress values--138, 172.4, 207, and 241 MN/m^2 (20, 25, 30, and 35 ksi). The data were represented by parallel straight lines indicating that the rate-controlling thermal-activation process is independent of stress level. From the least-squares slopes of these lines, an average value of 2.23×10^5 J/mole (54 kcal/mole) was obtained for Q_a, the apparent activation energy of creep.

$Ti_3Al + 10$ Nb. Figure 25 is an Arrhenius plot showing the temperature dependence of $\dot{\varepsilon}_s$ for Ti_3Al + 10 Nb for two stress values--312 and 138 MN/m^2 (45 and 20 ksi). The data corresponding to the 312 MN/m^2 stress could be represented by two straight lines having different slopes. Above ~ 650°C the straight line had a larger slope; from a least-square calculation, an apparent activation energy, Q_a, of ~ 3.1×10^5 J/mole (75 kcal/mole) was obtained. Below ~ 650°C, the straight line had a smaller slope yielding Q_a = ~ 1.9×10^5 J/mole (45 kcal/mole). For a stress value of 138 MN/m^2, the creep runs were made only in the 700-825°C range, the creep strains being extremely small below 700°C because of the low stress utilized. The data could be represented by a straight line which was very nearly parallel to the straight line for 312 MN/m^2 creep runs above ~ 650°C. Thus, above ~ 650°C, Q_a appears to be independent of stress. Below 650°C, a lower-activation-energy creep mechanism appears to be rate controlling.

Stress Dependence of Steady-State Creep Rates

Ti_3Al. In Fig. 26, values of $\dot{\varepsilon}_s$ for Ti_3Al are plotted as a function of ln (σ/E) for temperatures varying from 650 to 800°C. The temperature dependence of Young's modulus has been reported for Ti_3Al and Ti_3Al + 10 Nb

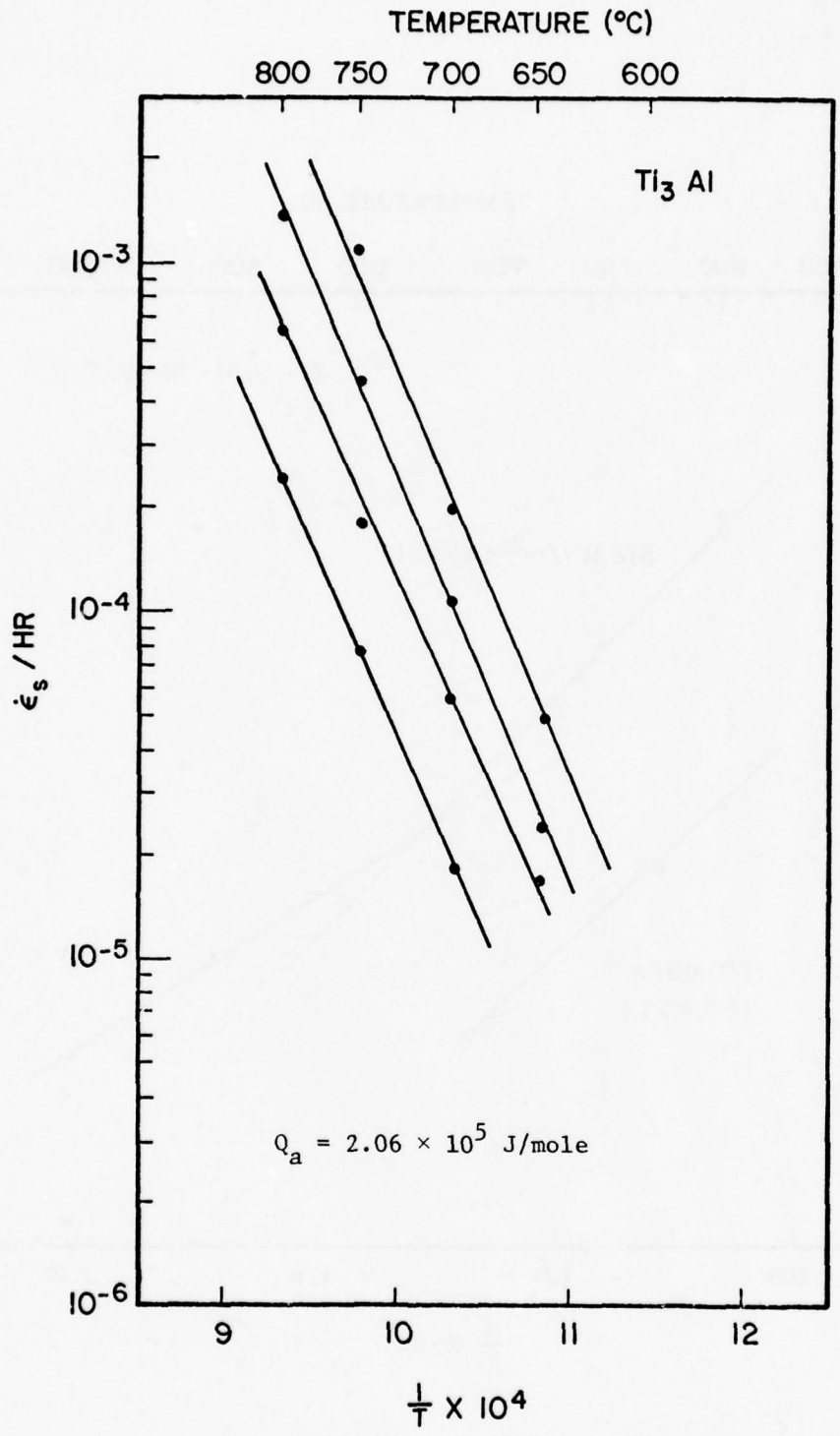

Figure 24. Temperature Dependence of Steady-State Creep Rate

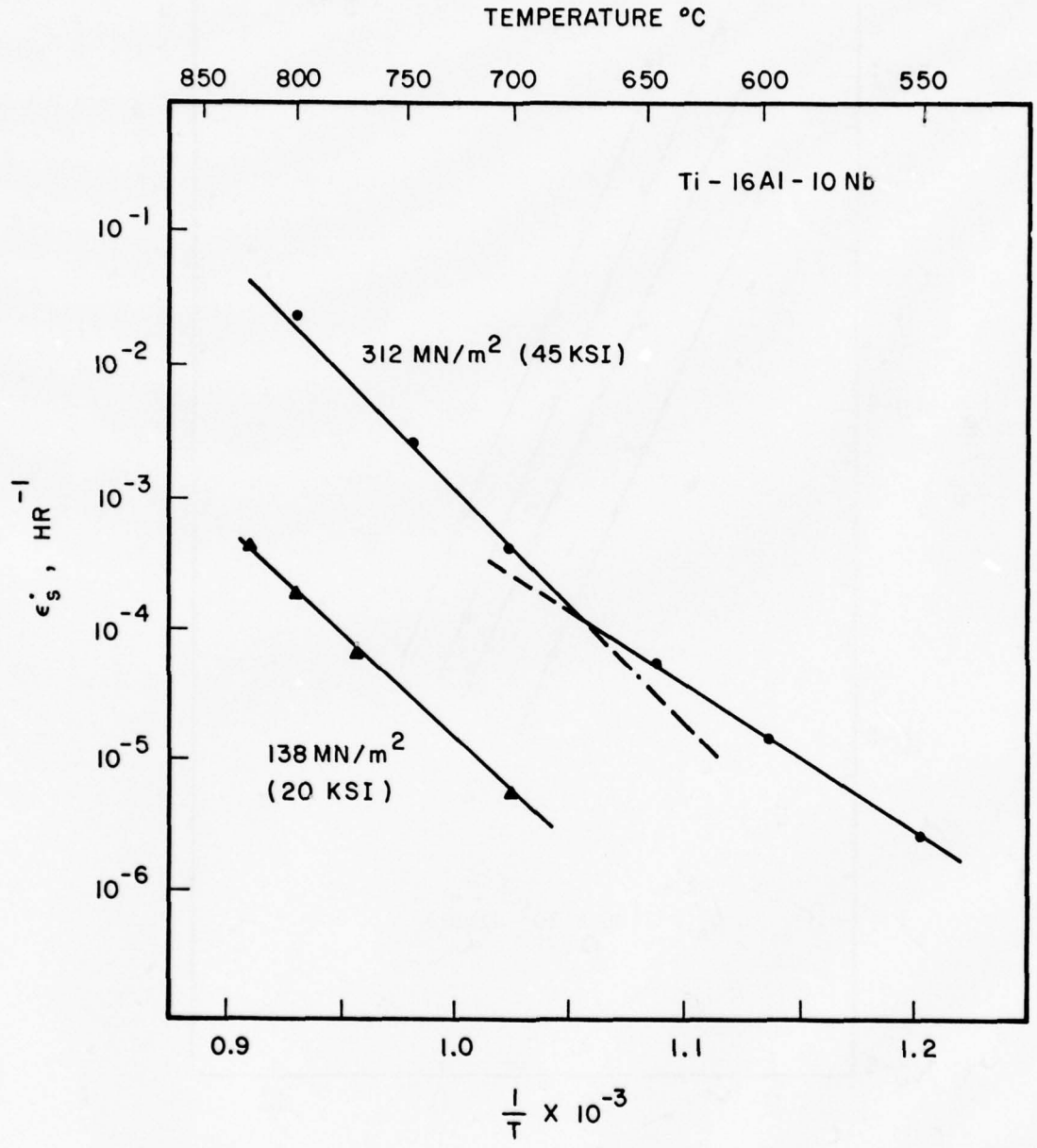

Figure 25. Temperature Dependence of Steady-State Creep Rate for Ti_3Al + 10 wt% Nb

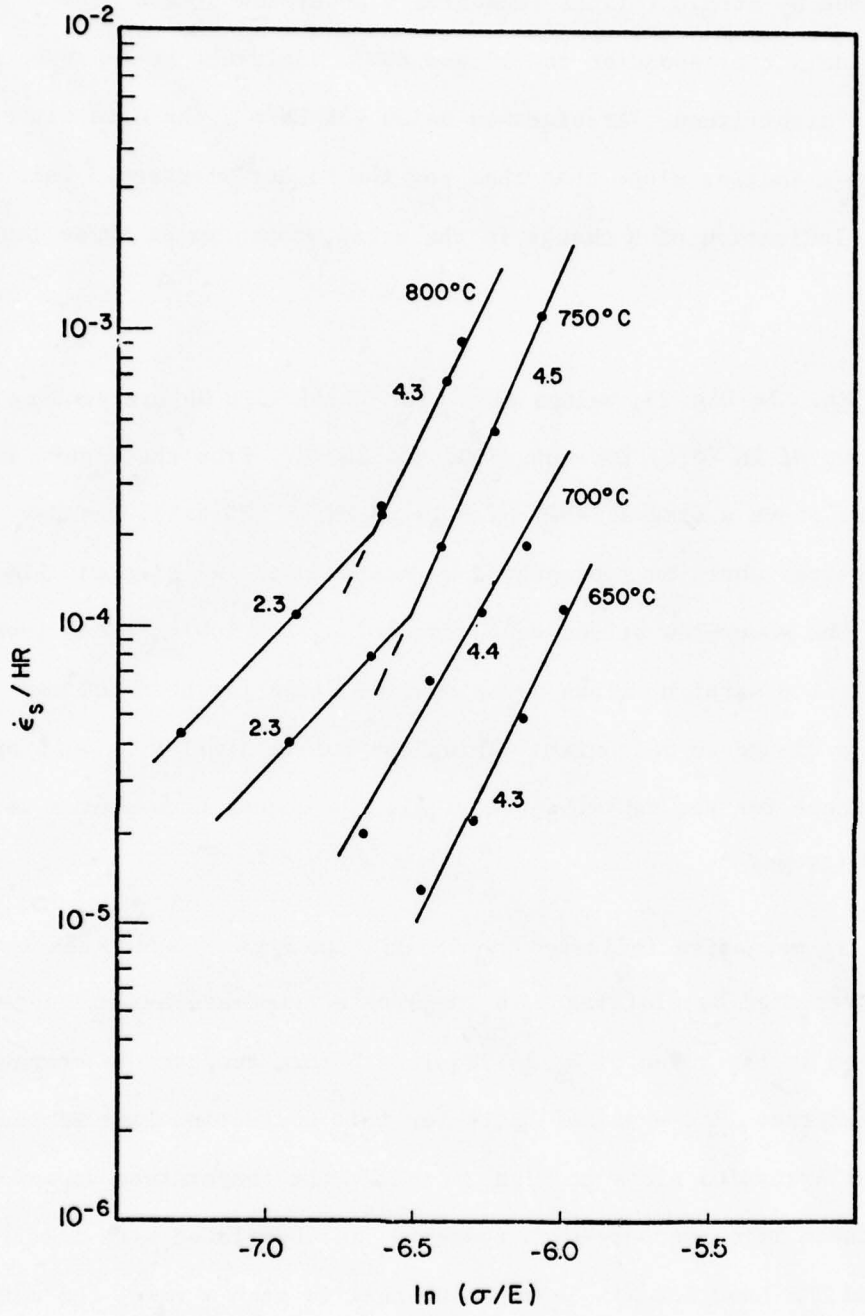

Figure 26. Stress Dependence of Steady-State Creep Rate for Ti_3Al

over the temperature range 25-940°C.[40] The fact that the creep data could be represented by straight lines indicates a power-law stress dependence of $\dot{\varepsilon}_s$. The data corresponding to 750 and 800°C could not be represented by single straight lines. At stresses below 138 MN/m^2, the data fit straight lines having a smaller slope than that for the higher stresses. This is taken as an indication of a change in the creep mechanism at these low stresses.

<u>Ti_3Al + 10 Nb</u>. In Fig. 27, values of $\dot{\varepsilon}_s$ for Ti_3Al + 10 Nb are plotted as a function of ln (σ/E) for 600, 700, and 800°C. From the figure it can be seen that above a stress level of ~ 172.5 MN/m^2 (25 ksi), the data for all temperatures could be represented by nearly parallel straight lines, indicating the power-law stress dependence of $\dot{\varepsilon}_s$. Below a stress level of 172.5 MN/m^2, the straight lines had a smaller slope for both 800 and 700°C, indicating a change in mechanism. This behavior is similar to that observed in Ti_3Al except for the fact that in Ti_3Al, the change occurs at a stress level of ~ 138 MN/m^2.

The change in mechanism indicated by the data in Figs. 26 and 27 can be better represented by plotting $\dot{\varepsilon}$ vs (σ/E) on a temperature-compensated basis. A correction in the value of Q_a is required before temperature compensation can be attempted. The physical basis for this correction lies in the fact that in the Arrhenius plots of Figs. 24 and 25, the temperature dependence of E is not taken into account--even though $\dot{\varepsilon}_s$ is correlated with σ/E(T) in Figs. 26 and 27. Lund and Nix[41] have shown that in such a case, the activation energy for creep, Q_c, is given by

$$Q_c = Q_a + nR \frac{T^2}{E} \times \frac{dE}{dT} \qquad (7)$$

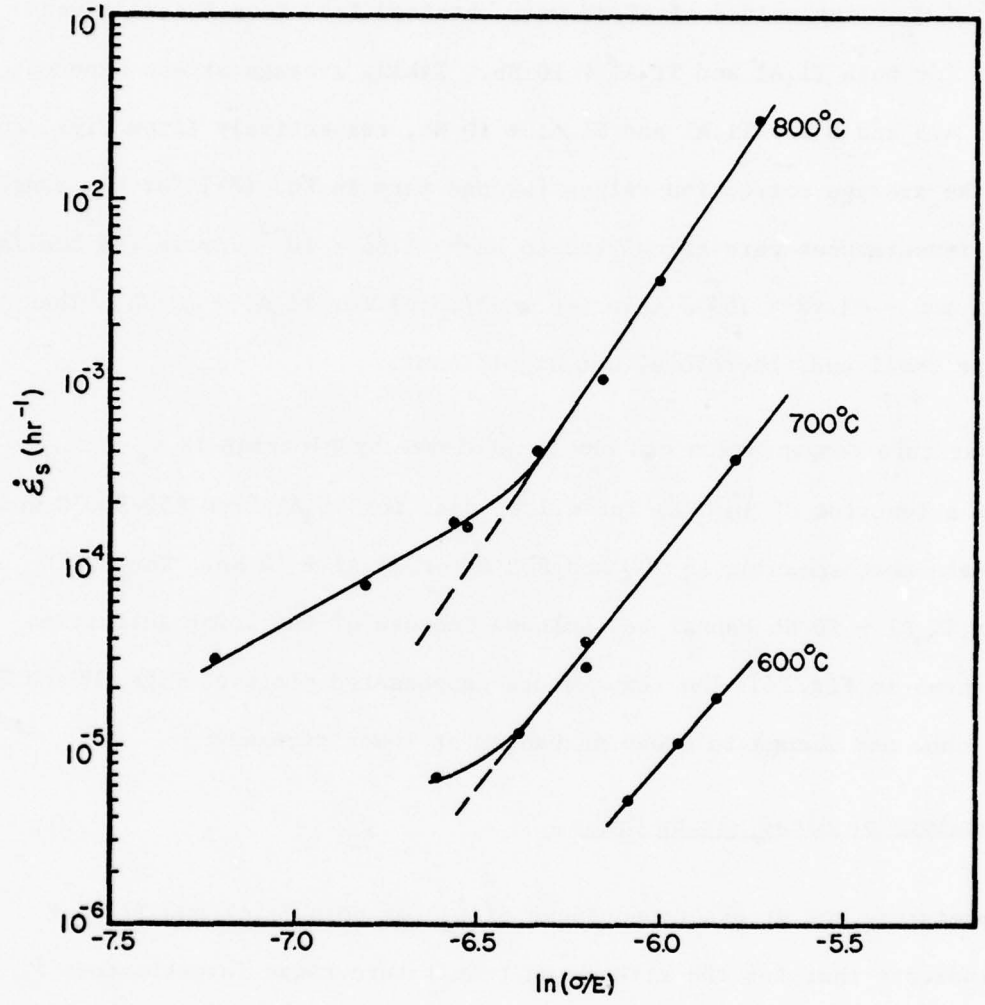

Figure 27. Normalized Stress Dependence of Steady-State Creep Rate for Ti_3Al + 10 wt% Nb

where Q_a is defined (as before) as the apparent activation energy obtained from an Arrhenius plot, n is the normalized stress exponent, R the gas constant, T the absolute temperature, and dE/dT the temperature dependence of Young's modulus. The value of dE/dT for most materials is negative; hence, $Q_c < Q_a$. The values of dE/dT were obtained from E-vs-T data given in Ref. 40 for both Ti_3Al and Ti_3Al + 10 Nb. Taking average stress exponent values of 4.5 and 6 for Ti_3Al and Ti_3Al + 10 Nb, respectively (from Figs. 26 and 27), the average correction values [second term in Eq. (7)] for the range of creep temperatures were calculated to be ~ -1.65×10^{-4} J/mole (-4 kcal/mole) for Ti_3Al and ~ -2.48×10^{4} J/mole (-6 kcal/mole) for Ti_3Al + 10 Nb. These values are small and, therefore, not significant.

The temperature compensation can now be achieved by plotting $\ln \dot{\varepsilon}_s + Q_c/RT$ as a function of $\ln(\sigma/E)$ for all $\dot{\varepsilon}_s$ data for Ti_3Al from 650-800°C and for $\dot{\varepsilon}_s$ data corresponding to 700 and 800°C for Ti_3Al + 10 Nb. The 600°C data for Ti_3Al + 10 Nb cannot be included because of the lower activation energy shown in Fig. 24. The temperature-compensated plots of Figs. 28 and 29 clearly show the change in creep mechanism at lower stresses.

Phenomenology of Steady-State Creep

The temperature and stress dependences of $\dot{\varepsilon}_s$ for both Ti_3Al and Ti_3Al + 10 Nb indicate that for the stress and temperature range investigated, $\dot{\varepsilon}_s$ can be described by

$$\dot{\varepsilon}_s \propto (\sigma/E)^n \exp(-Q_c/RT) \qquad (8)$$

Creep in Ti_3Al is characterized by an activation energy of 2.06×10^5 J/mole (50 kcal/mole) at all stresses and temperatures. The stress exponent, n, has

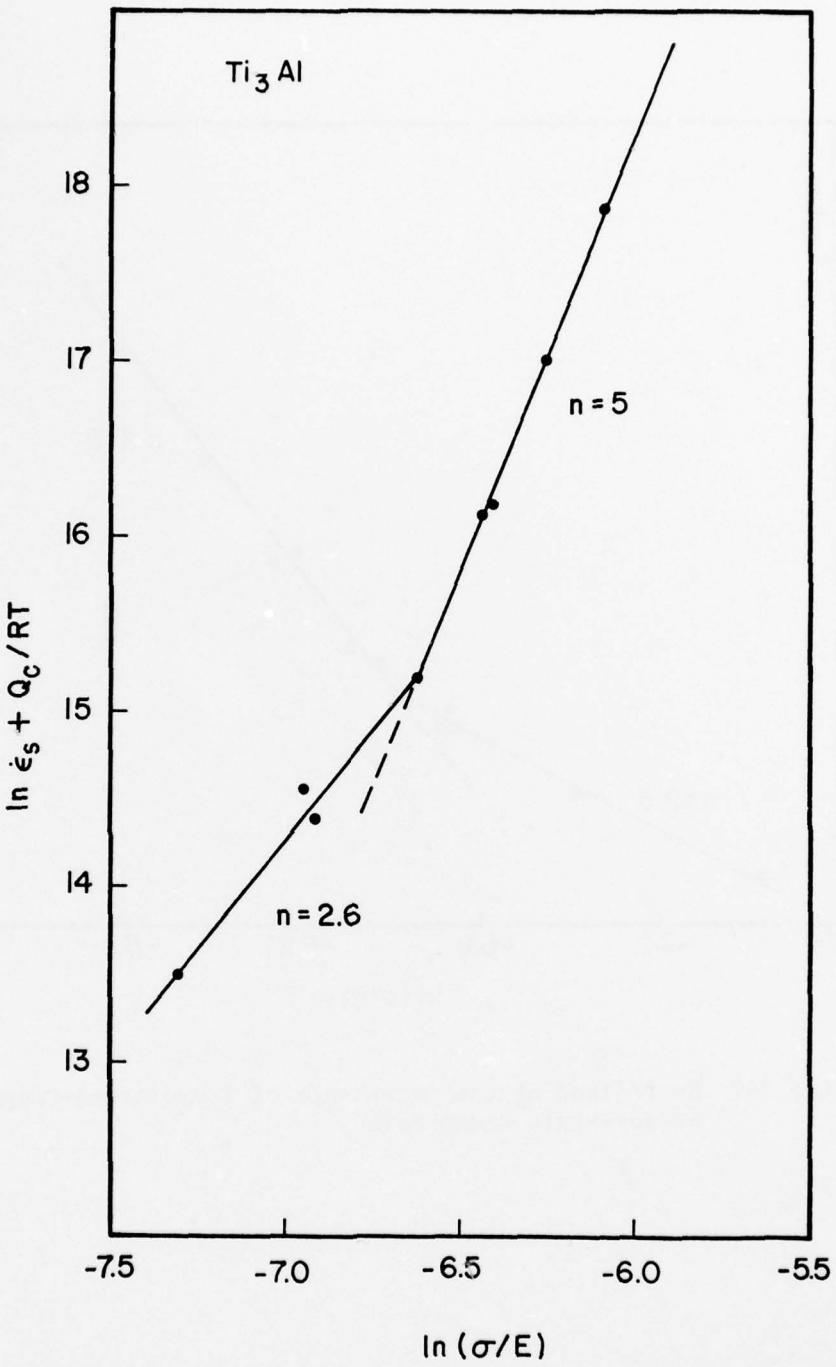

Figure 28. Stress Dependence of Temperature-Compensated Steady-State Creep Rate

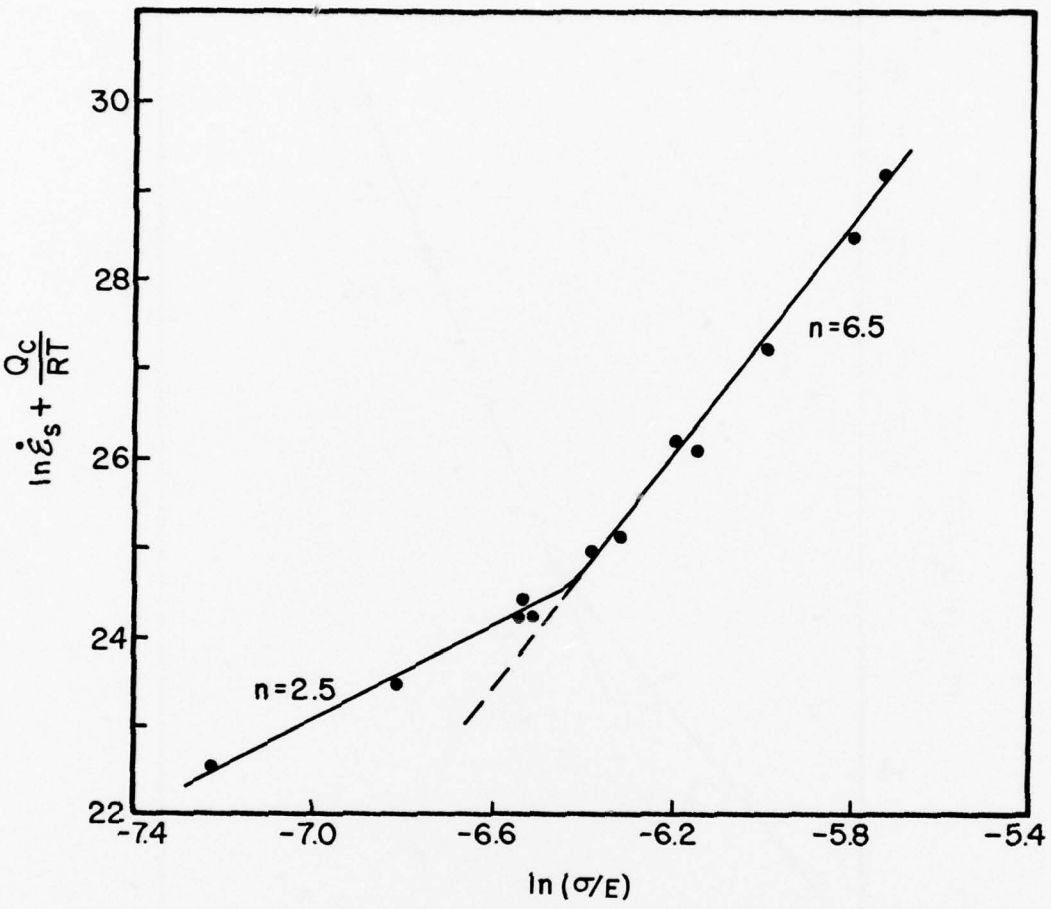

Figure 29. Normalized Stress Dependence of Temperature-Compensated Steady-State Creep Rate

a value of 4.3 - 5 at stresses above ~ 138 MN/m^2 (20 ksi). At temperatures at and above 750°C and at stresses below ~ 138 MN/m^2, the stress exponent has a value of 2.3 - 2.5.

For Ti_3Al + 10 Nb above 650°C, creep is characterized by an activation energy of 2.85×10^5 J/mole (69 kcal/mole). Two distinct rate-controlling creep mechanisms are indicated above 650°C--one mechanism having an n value of 6.5 above 172.5 MN/m^2 (25 ksi) stress and another having an n value of 2.5 below a stress value of 172.5 MN/m^2. Below 650°C the creep is controlled by yet another activated process having an activation energy of ~ 1.9×10^5 J/mole (45 kcal/mole) and a stress exponent of 5.5.

Dislocation Substructures

Temperature Dependence of the Substructures

Ti_3Al. Figure 30 (a-c) contains bright-field transmission electron micrographs showing dislocation structures in specimens deformed at a stress value of 276 MN/m^2 (40 ksi) and at temperatures of 600, 700, and 800°C, respectively. The major dislocation activity involved <a>-type dislocations on prism planes, and the common features observed were: segments of hexagonal dislocation networks formed by interactions between $<\bar{a}>$-type dislocations and long screw dislocations containing jogs and cusps. The interactions between dislocations increased with increasing temperature. The presence of jogs and cusps on screw dislocations suggests that a diffusion creep process is active in the temperature range studied.

In addition to the activity of $<\bar{a}>$ dislocations, unusual dislocation features were also observed in specimens deformed above 650°C. A detailed

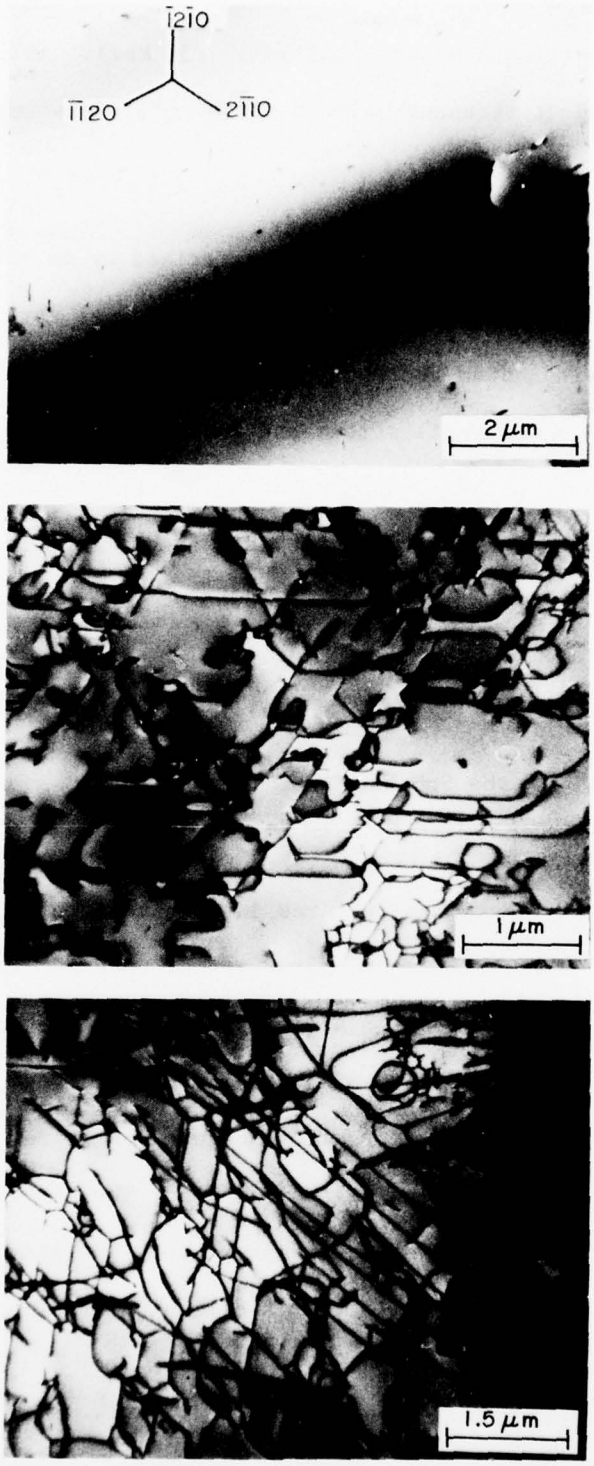

Figure 30. General Dislocation Structures in Creep Deformed Ti_3Al. (a) 600°C, 40 ksi; (b) 700°C, 40 ksi; (c) 800°C, 40 ksi. Foil Normal [0001]

presentation and analysis of these features is included in another paper.[42] These features were: 1) non-$\langle\bar{a}\rangle$-type dislocations, and 2) stacking faults with a $\langle\bar{p} + \frac{1}{2}\bar{c}\rangle$ displacement vector. The non-$\langle\bar{a}\rangle$-type dislocations have been identified as $[\bar{c}]$ dislocations.[42] These $[\bar{c}]$ dislocations were found to be highly jogged, straight dislocations. The stacking faults were analyzed and found to be intrinsic in nature, and the fault plane was found to be (0001).[42] The $\langle\bar{p} + \frac{1}{2}\bar{c}\rangle$ stacking faults may result from the dissociation of the $[\bar{c}]$ dislocations.[43] The presence of jogged $[\bar{c}]$ dislocations and the stacking faults again indicates that a diffusive process is operative during creep. The movement of $[\bar{c}]$ dislocations is probably accomplished by a climb process since their glide is not energetically favored.[43]

Ti_3Al + 10 Nb. Figure 31 (a) shows the creep substructure in specimens deformed at 600°C. The substructure consisted of hexagonal networks formed by $\langle\bar{a}\rangle$-type superdislocations. The results of the Burgers-vector analysis indicated that the hexagonal nets are formed by the following dislocation reaction:

$$\frac{1}{6}[2\bar{1}\bar{1}0] + \frac{1}{6}[\bar{1}2\bar{1}0] \rightarrow \frac{1}{6}[11\bar{2}0].$$

Figure 31 (b) is a schematic diagram of this reaction. $\frac{1}{6}\langle 10\bar{1}0\rangle$ extended dislocations were also observed in this reaction. The presence of extended dislocations in Ti_3Al + 10 Nb (and not in Ti_3Al) indicated a lowering of stacking-fault energy due to the addition of Nb in Ti_3Al. However, the tendency to form superdislocation networks was observed only in specimens crept at 600°C and not at higher temperatures. The thermal fluctuations at higher temperatures (> 600°C) appear to aid in the movement of unit dislocations

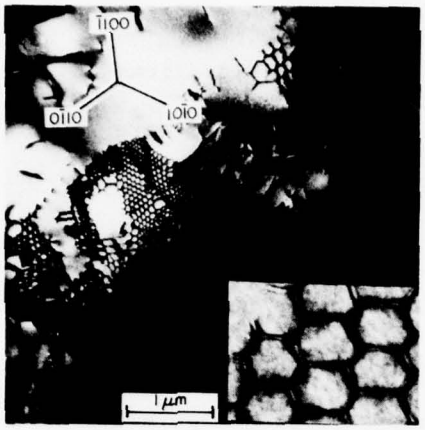

(a)

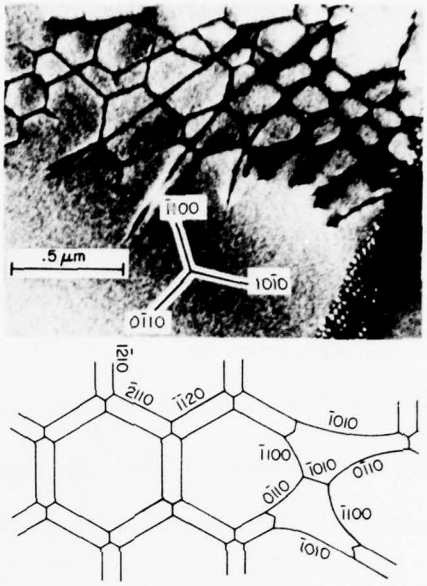

(b)

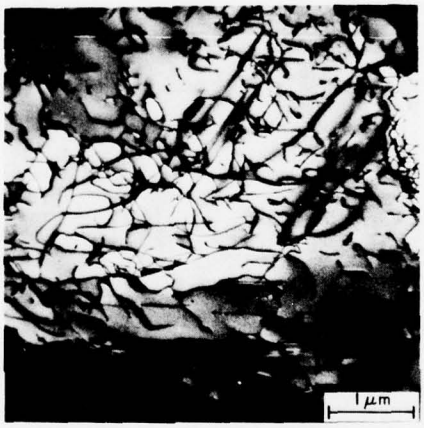

(c)

Figure 31. (a) Ti_3Al + 10 wt% Nb Creep Deformed at 608°C, 45 ksi
(b) A Sketch of the Hexagonal Nets Formed $\langle \bar{a} \rangle$ Superdislocations. $\frac{1}{b}\langle 10\bar{1}0 \rangle$ extended dislocations are also revealed.
(c) Dislocation Structures in Sample Creep Deformed at 750°C, 45 ksi

without the necessity for glide of either superdislocations or extended dislocations. In another study no extended dislocations were observed in Ti_3Al + 10 Nb specimens deformed in tension at 700°C.[35]

The arrangement and distribution of $\langle\bar{a}\rangle$ dislocations in Ti_3Al + 10 Nb specimens deformed at temperatures higher than 700°C was similar to that in Ti_3Al, namely, long screw dislocations with cusps and jogs and small segments of hexagonal networks, Fig. 31 (c). Non-$\langle\bar{a}\rangle$-type dislocations, $[\bar{c}]$ dislocations and $\langle\bar{p} + \frac{1}{2}\bar{c}\rangle$-type stacking faults were observed in higher densities in Ti_3Al with Nb than in Ti_3Al. These features, although not labeled, are shown in Fig. 32. The higher density of the $\langle\bar{p} + \frac{1}{2}\bar{c}\rangle$ stacking faults which form by the dissociation of $[\bar{c}]$ dislocations is another indication that Nb additions lower the stacking-fault energy of Ti_3Al. The microstructural differences between specimens creep deformed below and above 650°C correlate with the activation-energy differences. Creep below 650°C had an apparent activation energy of 1.9×10^5 J/mole, while that above 650°C was 2.85×10^5 J/mole.

Stress Dependence of the Substructure

Both Ti_3Al and Ti_3Al with Nb exhibited a change in creep mechanism with stress at temperatures above 700°C (Figs. 26 and 27). A distinct difference in creep microstructure was observed for stresses above and below 138 and 172 MN/m^2 for Ti_3Al and Ti_3Al + 10 Nb, respectively. Figure 33 shows the low-stress creep substructure in Ti_3Al. The substructure consisted of $\langle\bar{a}\rangle$ dislocation sub-boundaries with very low dislocation densities within the subgrains. Some small segments of $\langle\bar{c} + \bar{a}\rangle$-type dislocations were identified within the subgrains. The low-stress substructure may be compared to the high-stress substructure [Fig. 30 (b) and (c)]. The latter consisted of a

Figure 32. Stacking Fault in Creep Deformed Ti_3Al + 10 wt% Nb (750°C, 45 ksi)

Figure 33. General Dislocation Substructure in Creep-Deformed Ti_3Al (800°C, 20 ksi)

high density of complex three-dimensional dislocation arrangements similar to those exhibited by high-strength austenitic steels.[44]

The temperature and stress dependences of the steady-state creep rates appear to correlate reasonably well with development of creep-deformation microstructures in both Ti_3Al and Ti_3Al + 10 Nb. This indicates that distinct diffusion and/or dislocation mechanisms are rate controlling in different stress and temperature regimes. However, it is difficult to identify the particular creep mechanism which is operative; this difficulty stems primarily from the unavailability of diffusion data for Ti_3Al-base intermetallics. At present the creep-activation energies cannot be compared to those for diffusion. At high temperatures and stresses, activation energies of 2.06×10^5 J/mole (50 kcal/mole) and 2.85×10^5 J/mole (69 kcal/mole) for Ti_3Al and Ti_3Al + 10 Nb, respectively, and the stress exponent values of 4 - 6 indicate that dislocation climb is the most probable rate-controlling process. The change in mechanism indicated at low stresses may be, in fact, a transition regime, and at very low stresses and high temperatures grain-boundary sliding may be the rate-controlling mechanism.

CONCLUSIONS

The creep activation energy for Ti_3Al was found to be 2.06×10^5 J/mole (50 kcal/mole) for the stress and temperature range investigated. Addition of Nb increased the activation energy to a value of 2.85×10^5 J/mole (69 kcal/mole) for creep above 650°C and decreased it to a value of 1.9×10^5 J/mole (45 kcal/mole) for creep below 650°C.

The stress exponent for both intermetallics was found to be stress dependent at high temperatures. For Ti_3Al, the stress exponent had a value

of 4.3 - 5 above 138 MN/m^2 (20 ksi) and 2.3 - 2.5 below 138 MN/m^2, while for Ti_3Al + 10 Nb the stress exponent had a value of 6.5 above 172.5 MN/m^2 (25 ksi) and 2.5 below 172.5 MN/m^2. At low temperatures the stress exponent was found to be independent of stress for both materials, having values of 4.3 - 5 and 6.5 for Ti_3Al and Ti_3Al + 10 Nb, respectively.

The development of creep-dislocation microstructures correlated well with different creep regimes, as characterized by different stress and temperature dependences of the steady-state creep rates. However, due to nonavailability of diffusion data at present, it was not possible to identify the rate controlling creep mechanisms in these intermetallics.

REFERENCES

1. B. Lawn and R. Wilshaw, J. Mater. Sci. 10, 1049 (1975).

2. B. R. Lawn and M. V. Swain, J. Mater. Sci. 10, 113 (1975).

3. B. R. Lawn and E. R. Fuller, J. Mater. Sci. 10, 2016 (1975).

4. B. R. Lawn, E. R. Fuller, and S. M. Wiederhorn, J. Amer. Ceram. Soc. 59, 193 (1976).

5. A. G. Evans and T. R. Wilshaw, Acta Met. 24, 939 (1976).

6. R. H. Keays, A Review of Stress Intensity Factors for Surface and Internal Cracks, Structures and Materials Report 343 (Department of Supply, Australian Defence Scientific Service, Aeronautical Research Laboratories, April 1973).

7. A. E. Green and I. N. Sneddon, Proc. Cambridge Phil. Soc. 46, 159 (1950).

8. G. R. Irwin, J. Appl. Mech. 29, Trans. ASME 84, Series E, 651 (1962).

9. F. W. Smith, A. F. Emery, and A. S. Kobayashi, J. Appl. Mech. 34, Trans. ASME 89, Series E, 953 (1967).

10. R. C. Shah and A. S. Kobayashi, "Stress Intensity Factor for an Elliptical Crack Approaching the Surface of a Plate in Bending," in Stress Analysis and Growth of Cracks, Proceedings of the 1971 National Symposium on Fracture Mechanics, Part I, ASTM STP 513 (American Society for Testing and Materials, Philadelphia, PA, 1972), pp. 3-21.

11. M. A. Schroedl and C. W. Smith, "Local Stresses near Deep Surface Flaws under Cylindrical Bending Fields," in Progress in Flaw Growth and Fracture Toughness Testing, ASTM STP 536 (American Society for Testing and Materials, Philadelphia, PA, 1973), pp. 45-63.

12. J. J. Petrovic and L. A. Jacobson, "The Strength of Silicon Nitride after Exposure to Different Environments," in Ceramics for High-Performance Applications (J. J. Burke, A. E. Gorum, and R. N. Katz, eds.), Proceedings of the Second Army Materials Technology Conference, 13-16 November 1973, Hyannis, MA (Brook Hill Publishing Co., Chestnut Hill, MA, 1974).

13. J. J. Petrovic, L. A. Jacobson, P. K. Talty, and A. K. Vasudevan, J. Amer. Ceram. Soc. 58, 113 (1975).

14. R. R. Wills, M. G. Mendiratta, and J. J. Petrovic, J. Mater. Sci. 11, 1330 (1976).

15. J. J. Petrovic and L. A. Jacobson, J. Amer. Ceram. Soc. 59, 34 (1976).

16. N. Ingelstrom and H. Nordberg, Eng. Frac. Mech. 6, 597 (1974).

17. R. K. Govila, Acta Met. 20, 447 (1972).

18. J. J. Petrovic and M. G. Mendiratta, J. Amer. Ceram. Soc. 59, 163 (1976).

19. J. J. Petrovic and M. G. Mendiratta, J. Amer. Ceram. Soc. 60, 463 (1977).

20. M. G. Mendiratta, J. Wimmer, and I. Bransky, J. Mater. Sci. 12, 212 (1977).

21. M. G. Mendiratta and J. J. Petrovic, "Slow Crack Growth from Controlled Surface Flaws in Hot-Pressed Si_3N_4," Accepted for publication in the May-June 1978 issue of the Journal of the American Ceramic Society.

22. P. L. Land and M. G. Mendiratta, J. Mater. Sci. 12, 1421 (1977).

23. J. J. Petrovic, R. A. Dirks, L. A. Jacobson, and M. G. Mendiratta, J. Amer. Ceram. Soc. 59, 177 (1976).

24. J. B. Wachtman, Jr., W. Capps, and J. Mandel, J. of Mat., JMLSA, 7, 188 (1972).

25. A. Rudnick, A. R. Hunter, and F. C. Holden, Mat. Res. and Stand. 3, 283 (1963).

26. A. F. McLean, ASME Publication 70-GT-105 (American Society of Mechanical Engineers, New York, May 1970).

27. D. J. Godfrey, J. Brit. Interplanet. Soc. 22, 353 (1969).

28. D. C. Larsen, "Property Screening and Evaluation of Ceramic Vane Materials," Report No. IITRI-D6114-ITR-18 (Interim Technical Report No. 3), Air Force Contract F33615-75-C-5196, 26 February 1977.

29. R. W. Rice, "Fracture Topography of Ceramics," in Surfaces and Interfaces of Glass and Ceramics (V. D. Frechette, W. C. LaCourse, and V. L. Burdick, eds.)(Plenum Publishing Co., New York, 1974).

30. W. F. Brown, Jr., and J. E. Srawley, ASTM STP 410 (American Society for Testing and Materials, Philadelphia, PA, 1967), pp. 1-15.

31. R. R. Wills, M. G. Mendiratta, and J. J. Petrovic, J. Mater. Sci. 11, 1330 (1976).

32. N. S. Choudhury, H. C. Graham, and J. W. Hinze, "Oxidation Behavior of Titanium Aluminides," in Proceedings of the Symposium on Properties of High Temperature Alloys (Electrochemical Society, Princeton, NJ, March 1977), pp. 668-680.

33. H. A. Lipsitt, R. E. Schafrik, and D. Schechtman, private communication.

34. J. C. Williams and M. J. Blackburn, in Ordered Alloys (H. Kear, T. Sims, S. Stoloff, and J. H. Westbrook, eds.)(Claitor's Publishing Division, Baton Rouge, LA, 1970), pp. 425-445.

35. S. M. L. Sastry and H. A. Lipsitt, Met. Trans. 8A, 1543 (1977).

36. S. M. L. Sastry and H. A. Lipsitt, Acta Met. 25, 1279 (1977).

37. N. S. Choudhury and J. E. Henry, unpublished research.

38. H. A. Lipsitt, D. Schechtman, and R. E. Schafrik, Met. Trans. 6A, 1991 (1975).

39. M. J. Blackburn and J. C. Williams, Trans. TMS-AIME 239, 187 (1967).

40. R. W. Schafrik, Met. Trans. 8A, 1003 (1977).

41. R. W. Lund and W. D. Nix, Met. Trans 6A, 1329 (1975).

42. W. J. Yang, J. C. Williams, M. G. Mendiratta, and H. A. Lipsitt, private communication.

43. W. J. Yang, private communication.

44. B. Modeer and R. Lagneborg, Jernkont. Ann. 155, 363 (1971).

☆U.S.Government Printing Office: 1978 — 757-080/133